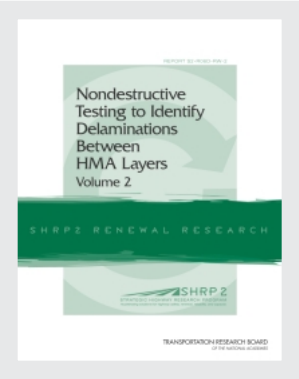

Nondestructive Testing to Identify Delaminations Between HMA Layers, Volume 2 - Theoretical Models

DETAILS

0 pages | 8.5 x 11 | PAPERBACK

ISBN 978-0-309-43447-8 | DOI 10.17226/22603

AUTHORS

Heitzman, Michael; Maser, Kenneth; Tran, Nam H.; Brown, Ray; Bell, Haley; Holland, Steve; Ceylan, Halil; Belli, Kimberly; and Hiltunen, Dennis

The Second
STRATEGIC HIGHWAY RESEARCH PROGRAM

SHRP 2 REPORT S2-R06D-RW-2

Nondestructive Testing to Identify Delaminations Between HMA Layers

Volume 2

Michael Heitzman
Kenneth Maser
Nam H. Tran
Ray Brown
Haley Bell
Steve Holland
Halil Ceylan
Kimberly Belli
Dennis Hiltunen

National Center for Asphalt Technology at Auburn University
Alabama

TRANSPORTATION RESEARCH BOARD

WASHINGTON, D.C.
2013
www.TRB.org

Subscriber Categories

Construction
Highways
Maintenance and Preservation
Pavements

The Second Strategic Highway Research Program

America's highway system is critical to meeting the mobility and economic needs of local communities, regions, and the nation. Developments in research and technology—such as advanced materials, communications technology, new data collection technologies, and human factors science—offer a new opportunity to improve the safety and reliability of this important national resource. Breakthrough resolution of significant transportation problems, however, requires concentrated resources over a short time frame. Reflecting this need, the second Strategic Highway Research Program (SHRP 2) has an intense, large-scale focus, integrates multiple fields of research and technology, and is fundamentally different from the broad, mission-oriented, discipline-based research programs that have been the mainstay of the highway research industry for half a century.

The need for SHRP 2 was identified in *TRB Special Report 260: Strategic Highway Research: Saving Lives, Reducing Congestion, Improving Quality of Life,* published in 2001 and based on a study sponsored by Congress through the Transportation Equity Act for the 21st Century (TEA-21). SHRP 2, modeled after the first Strategic Highway Research Program, is a focused, time-constrained, management-driven program designed to complement existing highway research programs. SHRP 2 focuses on applied research in four areas: Safety, to prevent or reduce the severity of highway crashes by understanding driver behavior; Renewal, to address the aging infrastructure through rapid design and construction methods that cause minimal disruptions and produce lasting facilities; Reliability, to reduce congestion through incident reduction, management, response, and mitigation; and Capacity, to integrate mobility, economic, environmental, and community needs in the planning and designing of new transportation capacity.

SHRP 2 was authorized in August 2005 as part of the Safe, Accountable, Flexible, Efficient Transportation Equity Act: A Legacy for Users (SAFETEA-LU). The program is managed by the Transportation Research Board (TRB) on behalf of the National Research Council (NRC). SHRP 2 is conducted under a memorandum of understanding among the American Association of State Highway and Transportation Officials (AASHTO), the Federal Highway Administration (FHWA), and the National Academy of Sciences, parent organization of TRB and NRC. The program provides for competitive, merit-based selection of research contractors; independent research project oversight; and dissemination of research results.

SHRP 2 Report S2-R06D-RW-2

ISBN: 978-0-309-27294-0

Copyright Information

Note: SHRP 2 report numbers convey the program, focus area, project number, and publication format. Report numbers ending in "w" are published as web documents only.

Notice

The project that is the subject of this report was a part of the second Strategic Highway Research Program, conducted by the Transportation Research Board with the approval of the Governing Board of the National Research Council.

The members of the technical committee selected to monitor this project and review this report were chosen for their special competencies and with regard for appropriate balance. The report was reviewed by the technical committee and accepted for publication according to procedures established and overseen by the Transportation Research Board and approved by the Governing Board of the National Research Council.

The opinions and conclusions expressed or implied in this report are those of the researchers who performed the research and are not necessarily those of the Transportation Research Board, the National Research Council, or the program sponsors.

The Transportation Research Board of the National Academies, the National Research Council, and the sponsors of the second Strategic Highway Research Program do not endorse products or manufacturers. Trade or manufacturers' names appear herein solely because they are considered essential to the object of the report.

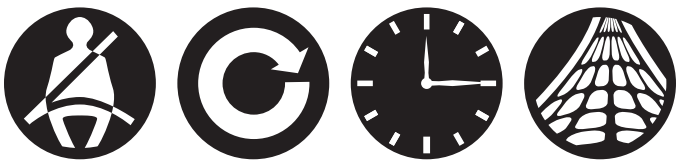

SHRP 2 Reports

Available by subscription and through the TRB online bookstore:

www.TRB.org/bookstore

Contact the TRB Business Office:
202-334-3213

More information about SHRP 2:

www.TRB.org/SHRP2

THE NATIONAL ACADEMIES

Advisers to the Nation on Science, Engineering, and Medicine

The **National Academy of Sciences** is a private, nonprofit, self-perpetuating society of distinguished scholars engaged in scientific and engineering research, dedicated to the furtherance of science and technology and to their use for the general welfare. On the authority of the charter granted to it by Congress in 1863, the Academy has a mandate that requires it to advise the federal government on scientific and technical matters. Dr. Ralph J. Cicerone is president of the National Academy of Sciences.

The **National Academy of Engineering** was established in 1964, under the charter of the National Academy of Sciences, as a parallel organization of outstanding engineers. It is autonomous in its administration and in the selection of its members, sharing with the National Academy of Sciences the responsibility for advising the federal government. The National Academy of Engineering also sponsors engineering programs aimed at meeting national needs, encourages education and research, and recognizes the superior achievements of engineers. Dr. Charles M. Vest is president of the National Academy of Engineering.

The **Institute of Medicine** was established in 1970 by the National Academy of Sciences to secure the services of eminent members of appropriate professions in the examination of policy matters pertaining to the health of the public. The Institute acts under the responsibility given to the National Academy of Sciences by its congressional charter to be an adviser to the federal government and, on its own initiative, to identify issues of medical care, research, and education. Dr. Harvey V. Fineberg is president of the Institute of Medicine.

The **National Research Council** was organized by the National Academy of Sciences in 1916 to associate the broad community of science and technology with the Academy's purposes of furthering knowledge and advising the federal government. Functioning in accordance with general policies determined by the Academy, the Council has become the principal operating agency of both the National Academy of Sciences and the National Academy of Engineering in providing services to the government, the public, and the scientific and engineering communities. The Council is administered jointly by both Academies and the Institute of Medicine. Dr. Ralph J. Cicerone and Dr. Charles M. Vest are chair and vice chair, respectively, of the National Research Council.

The **Transportation Research Board** is one of six major divisions of the National Research Council. The mission of the Transportation Research Board is to provide leadership in transportation innovation and progress through research and information exchange, conducted within a setting that is objective, interdisciplinary, and multimodal. The Board's varied activities annually engage about 7,000 engineers, scientists, and other transportation researchers and practitioners from the public and private sectors and academia, all of whom contribute their expertise in the public interest. The program is supported by state transportation departments, federal agencies including the component administrations of the U.S. Department of Transportation, and other organizations and individuals interested in the development of transportation. **www.TRB.org**

www.national-academies.org

SHRP 2 STAFF

Ann M. Brach, *Director*
Stephen J. Andrle, *Deputy Director*
Neil J. Pedersen, *Deputy Director, Implementation and Communications*
James Bryant, *Senior Program Officer, Renewal*
Kenneth Campbell, *Chief Program Officer, Safety*
JoAnn Coleman, *Senior Program Assistant, Capacity and Reliability*
Eduardo Cusicanqui, *Financial Officer*
Walter Diewald, *Senior Program Officer, Safety*
Jerry DiMaggio, *Implementation Coordinator*
Shantia Douglas, *Senior Financial Assistant*
Charles Fay, *Senior Program Officer, Safety*
Carol Ford, *Senior Program Assistant, Renewal and Safety*
Elizabeth Forney, *Assistant Editor*
Jo Allen Gause, *Senior Program Officer, Capacity*
Rosalind Gomes, *Accounting/Financial Assistant*
Abdelmename Hedhli, *Visiting Professional*
James Hedlund, *Special Consultant, Safety Coordination*
Alyssa Hernandez, *Reports Coordinator*
Ralph Hessian, *Special Consultant, Capacity and Reliability*
Andy Horosko, *Special Consultant, Safety Field Data Collection*
William Hyman, *Senior Program Officer, Reliability*
Michael Marazzi, *Senior Editorial Assistant*
Linda Mason, *Communications Officer*
Reena Mathews, *Senior Program Officer, Capacity and Reliability*
Matthew Miller, *Program Officer, Capacity and Reliability*
Michael Miller, *Senior Program Assistant, Capacity and Reliability*
David Plazak, *Senior Program Officer, Capacity*
Onno Tool, *Visiting Professional*
Dean Trackman, *Managing Editor*
Connie Woldu, *Administrative Coordinator*
Patrick Zelinski, *Communications/Media Associate*

ACKNOWLEDGMENTS

This work was sponsored by the Federal Highway Administration in cooperation with the American Association of State Highway and Transportation Officials. It was conducted in the second Strategic Highway Research Program, which is administered by the Transportation Research Board of the National Academies. The project was managed by Dr. Monica Starnes, Senior Program Officer for SHRP 2 Renewal.

The team recognizes the technical input of the research team's expert panel. In addition to providing the team with valuable comments, the highway agency team members assisted with identification and support of field evaluation sites. The members of the expert panel are Jim Musselman, the Florida Department of Transportation (DOT); Kim Willoughby, the Washington State DOT; Andrew Gisi, the Kansas DOT; Nadarajah Sivaneswaran, FHWA; John Harvey, University of California, Davis; and Harold Von Quintus, Applied Research Associates.

The team recognizes the support of the NDT technology firms that expended their own resources to provide NDT equipment and software to the study. The companies that supported the project were Geophysical Survey Systems, Inc.; MALA AB; 3d-Radar (a Curtiss-Wright Company); Geomedia Research and Development; Olson Instruments, Inc. and Olson Engineering Inc.; and Infrared Cameras, Inc. The study could not have been completed without their generous assistance.

The team especially recognizes the efforts of the hardware and software development staffs of 3d-Radar and Olson Instruments, Inc., for improving the capabilities of their NDT technologies to meet the needs of highway agencies.

FOREWORD

Monica A. Starnes, PhD, *Senior Program Officer, Renewal*

Asphalt pavements with delamination problems experience considerable early damage because delaminations provide paths for moisture damage and the development of damage such as stripping, slippage cracks, and pavement deformation. Early detection of the existence, extent, and depth of delaminations in asphalt pavements is key for determining the appropriate rehabilitation strategy and thus extending the life of the given pavement.

This report presents the findings of the first two phases of SHRP 2 Renewal Project R06D, Nondestructive Testing to Identify Delaminations Between HMA Layers. The main objective of the project was to develop nondestructive testing (NDT) techniques capable of detecting and quantifying delaminations in HMA pavements. The NDT techniques should be applicable to construction, project design, and network-level assessments.

During Phase 1 of the project, the research team evaluated NDT methods that could potentially detect the most typical delaminations in asphalt pavements. Both laboratory and field testing were conducted during this task. Based on the findings from this testing, the manufacturers of two promising technologies conducted further development of their products to meet the goals of this project in Phase 2. The two technologies advanced in this research were ground-penetrating radar (GPR) and impact echo/spectral analysis of surface waves (IE/SASW).

Additionally, the project developed guidelines and piloted both NDT technologies in collaboration with highway agencies. Once completed, the results from this additional scope of work will be published as an addendum to this report.

CONTENTS

CHAPTER 1

Theoretical Models for Ground-Penetrating Radar

The numerical simulations presented in this chapter were carried out by Infrasense with support from Dr. Kim Belli of Northeastern University in Boston, Professor Dennis Hiltunen of the University of Florida, and Professor Rajib Mallick of Worcester Polytechnic Institute.

Numerical simulations of nondestructive testing (NDT) techniques were carried out to assess the NDT ability to detect delaminations and to evaluate the most promising configurations for implementing each NDT method. An NDT technique and/or configuration that does not show promise in the numerical simulations would likely not succeed in the field evaluations; therefore, results obtained from the simulations would help the project team focus on the most promising methods and/or configurations in the laboratory and field evaluations.

The numerical simulations were conducted by using existing numerical models to simulate and compare simulation results of delaminated and intact pavements. The simulation information was used to define detectability and served to support recommendations of specific methods and/or configurations for the laboratory and field evaluations. Modeling provided insight into results that could be expected from laboratory and field experiments, and it offered guidance into the effective configurations of the transmitter (T) and receiver (R) for each NDT technique. Modeling results were considerably cleaner than results obtained in the laboratory and field evaluations, and the modeling results were based on certain idealizations of material characteristics and input signals. Simulation results showed (a) whether, under ideal conditions, the pavement defect can be detected and (b) under what conditions detectability can be enhanced. For electromagnetic and mechanical wave methods, the simulation results could show how the relative placement of the source and receiver could affect the NDT detectability.

Simulation Overview

A time-domain GPR antenna is typically used in highway and bridge evaluations. Therefore, Maxwell's time-dependent curl equations were used to model wave propagation in this GPR simulation. The simulation was conducted via a two-dimensional (2-D) finite difference time domain (FDTD) algorithm. The FDTD method explicitly discretized Maxwell's equations by using the finite difference approximation for the computation of differential equations. The electric field measurements from the 2-D FDTD simulation were analogous similar to the output from the GPR antenna. The FDTD method was also able to handle inhomogeneous materials of asphalt concrete.

To simulate GPR investigation of a pavement in two dimensions, the transverse magnetic (TM) mode was chosen with wave propagation in the x–y plane (TM_z). This mode had no magnetic field in the direction perpendicular to the cross-sectional geometry (z-direction). This perpendicular direction was assumed to be the polarization direction of the antenna.

Simulation Parameters

All GPR simulations were carried out by using a 2-D FDTD code. Discretization of the physical model was done at a resolution of 1 mm (0.04 in.) so that the thin delamination could be adequately modeled. The time step was selected to be 2 ps to meet stability requirements. The signals used to excite the models are shown in Figure 1.1. The modulated Gaussian pulse was centered at either 1.3 GHz or 2.6 GHz, and the –3dB bandwidth was chosen to be equal to the center frequency.

GPR Simulations for Intact Pavement

Typical 203-mm (8-in.) thick asphalt geometry (with no defects) is shown in Figure 1.2. Asphalt was assumed to have a dielectric

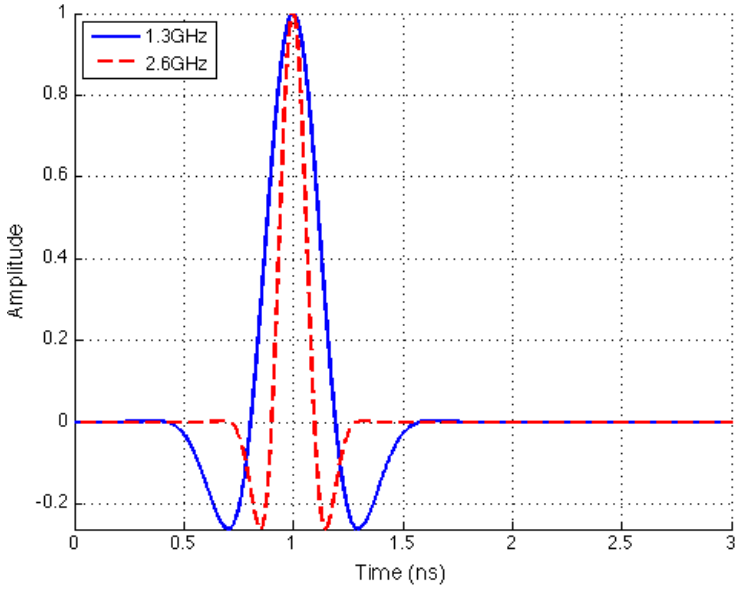

Figure 1.1. Simulation excitation signals (−3dB bandwidth equal to center frequency).

constant of 5, and it was not considered to be conductive. The geometry included a layer of air under the asphalt. This layer was expected to produce a higher reflection from the bottom of the asphalt layer than if it was over another medium (such as concrete or granular base). However, because the purpose of this simulation was to determine the reflection from the defects within the asphalt layer, it should not affect simulation results.

Note that the T and R locations were assumed to be at the surface of the asphalt. It was understood that configurations to be considered in this program would include air-launched antennae, but that the ground-coupled configuration would adequately represent the response for modeling purposes.

In the field, data would not be collected at every point in the structure. However, this information was available in a computational model and could be very helpful in determining what was going on in the responses recorded at the receivers. For the intact pavement, images of the electric field in the model at four different times are presented in Figure 1.3. The black horizontal lines indicate the boundaries of the asphalt pavement. Note that the 500-mm axis location in Figure 1.3 corresponds to the 0-cm transmitter location in Figure 1.2.

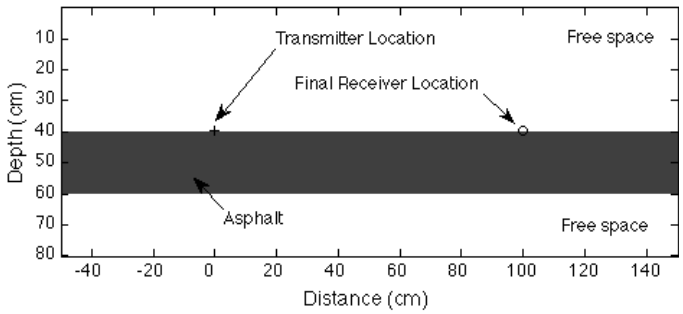

Figure 1.2. Simulation geometry for intact pavement: 3-mm-raised antenna is shown on the surface.

Move-Out Simulations

The move-out simulations were conducted to provide insight into (a) whether a defect was expected to be seen under ideal conditions and (b) how the reflection from the defect was expected to be observed at different transmitter and receiver configurations. For modeling purposes, a ground-coupled antenna configuration was represented, with two alternative vertical positions of the transmitter and receiver antennae: one directly on the asphalt surface, and the other elevated 3 mm (0.12 in.) above the asphalt surface. The simulations showed little difference between these two cases. Since the 3-mm (0.12-in.) elevation was more representative of an actual ground-coupled antenna, the results presented later were for that case.

Move-out simulations were conducted by assuming a fixed transmitter location and a variety of receiver locations moving out from the transmitter at 10-mm (0.4-in.) intervals. The defect condition geometries for the move-out simulations are shown in Figure 1.4. While the transmitter (+) and each of the receiver (o) locations were shown on the surface of the asphalt, the results presented were for the case where the antenna was 3 mm (0.12 in.) above the surface, as previously discussed. As shown in Figure 1.4, three delamination cases were simulated, including (1) 2-in (50-mm) deep, 1-mm (0.04-in.) thick delamination; (2) 4-in (100-mm) deep, 1-mm (0.04-in.) thick delamination; and (3) stripped asphalt layer between 3-in (75-mm) and 4-in (100-mm) depths. In

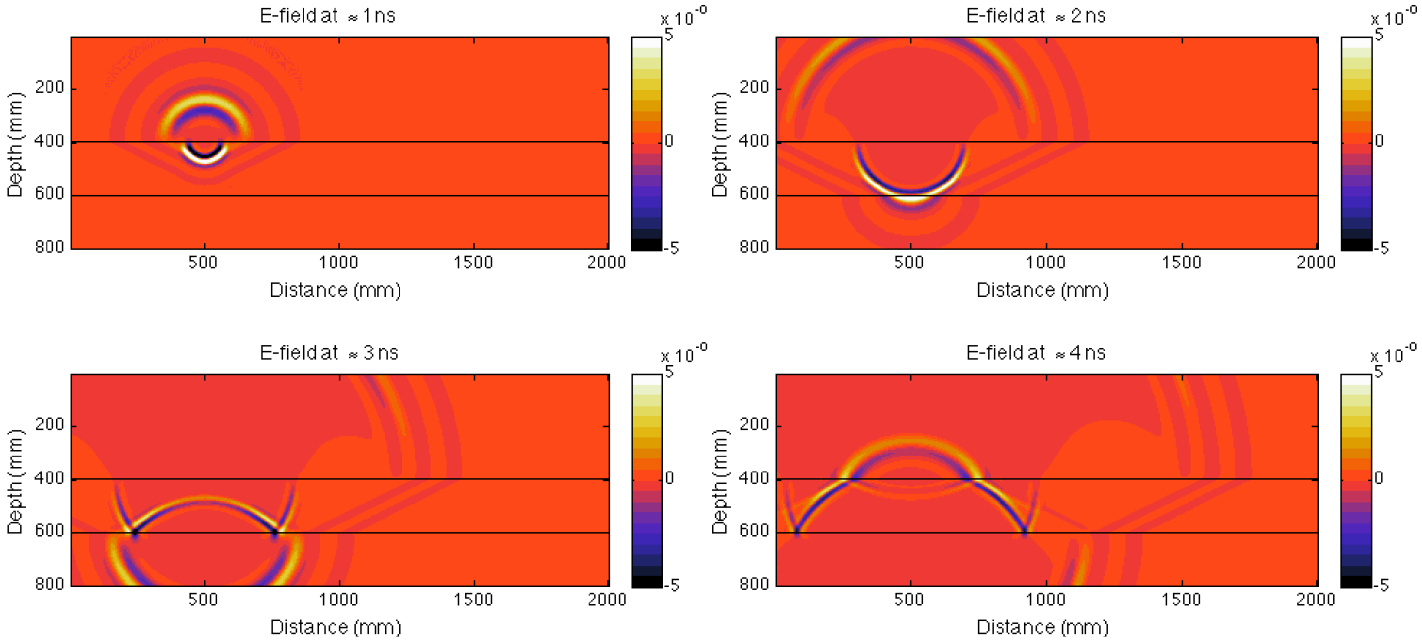

Figure 1.3. Electric field (E-field) throughout the modeled intact pavement at four given times for the surface 2.6 GHz excitation.

those cases, the dielectric constant of the stripped layer either was 3.5 (containing more air) or 9.0 (containing more water).

B-Scan Simulations

Instead of considering the fixed transmitter and moving receivers as in the move-out simulations, for the B-scan simulations, the distance between the transmitter (T) and receiver (R) was fixed, either 125 mm (5 in.) or 40 mm (1.6 in.), and they were moved across the pavement. This is the typical configuration for a single ground-coupled antenna that is moved across the surface of the pavement, and the resulting display is generally referred to as a B-scan. This configuration resulted in a single simulation run for each T/R location, and one run

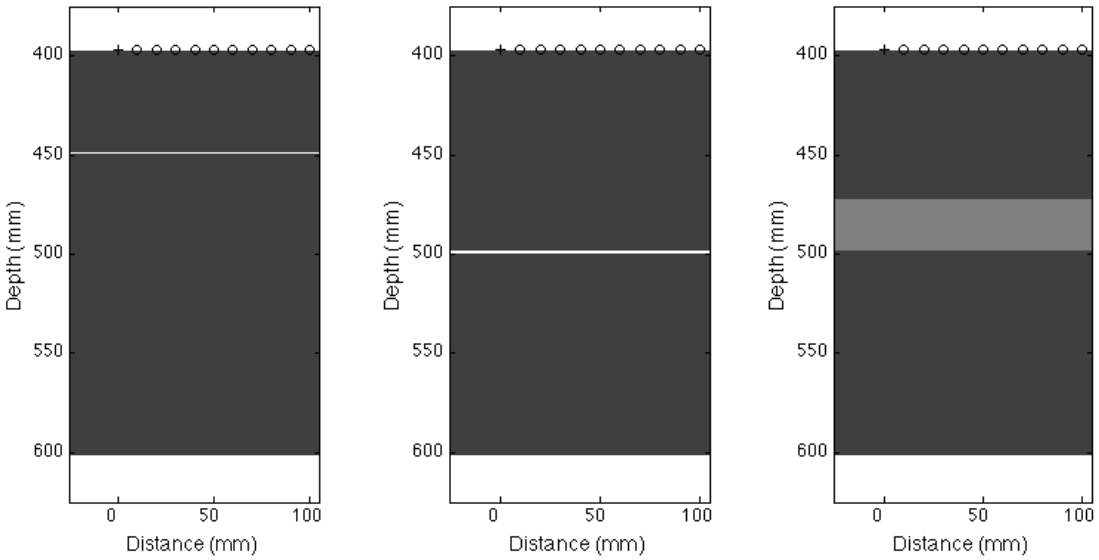

Note: The defect runs through the entire cross section of the model.

Figure 1.4. Move-out simulation geometries for (a) 2-in.-deep, 1-mm (0.04-in.) thick delamination; (b) 4-in.-deep, 1-mm (0.04-in.) thick delamination; and (c) stripped asphalt between depths of 3 in. and 4 in.

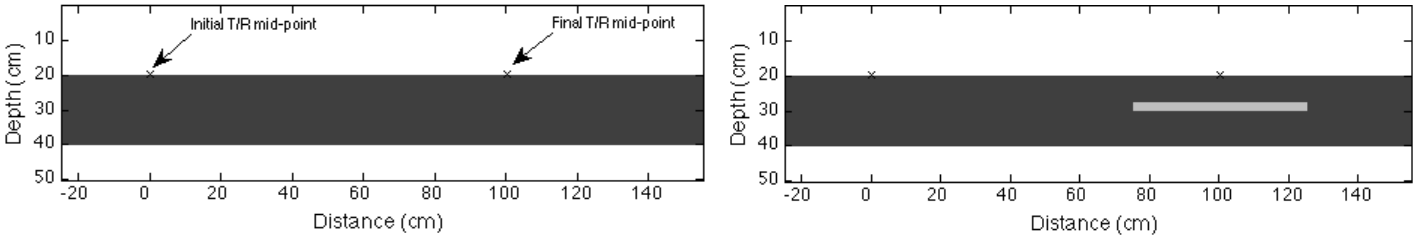

Note: Antenna is shown on the surface and geometries are similar for 3-mm raised antenna. Delamination geometries are not shown because at this scale, the representation of the delamination is difficult to see. Vertically, geometries are similar to those in Figure 1.4a and b, and, horizontally, to that in (b).

Figure 1.5. Example of B-scan simulation geometries for (a) intact case and (b) stripped asphalt 3–4 in. deep.

was carried out every 10 mm (0.4 in.) across the pavement. The T/R pair was located 3 mm (0.12 in.) above the surface. The B-scan geometries for intact and stripped pavements are shown in Figure 1.5. The initial and final T/R midpoints are shown in Figure 1.5a. Note that the T or R locations would change depending on whether the separation was 125 mm (5 in.) or 40 mm (1.6 in.), but all of the discussions would consider the midpoint. Since the geometry was symmetric, simulations were only run until the midpoint of the defect (100 cm or 39.4 in.) and then mirrored to construct the final B-scan. This procedure resulted in 101 simulations per case.

Simulation Results

Move-Out Simulations

Figure 1.6 shows the response recorded at each R for the intact and 2-in. delamination cases for the 2.6-GHz antenna model. The horizontal axis was the distance across the pavement from R to T, which was fixed and never moved. The response at approximately 1 ns, for the R located zero mm from the transmitter, was due to a direct signal and the reflection from the surface of the asphalt. The response at the same horizontal location and approximately 4 ns was the reflection from the bottom of the asphalt. As previously discussed, the asphalt was floating in free space so this bottom reflection was stronger than would be observed in the field. Since the most promising results were obtained by using the 2.6-GHz antenna model, these results are presented later in this report.

Figure 1.7a shows the 2.6-GHz antenna simulation for the case of the delamination at 4 in. The effect of the delamination at 4-in. depth shows up deeper (later in time) than does the effect for the 2-in.-deep delamination (Figure 1.6b). Figure 1.7b shows the Figure 1.7a results with the intact data of Figure 1.6a subtracted. The subtraction of the intact data highlights the effect of the delamination.

Figure 1.7b shows that the amplitude of the reflection from the delamination increases as the receiving antenna is moved from

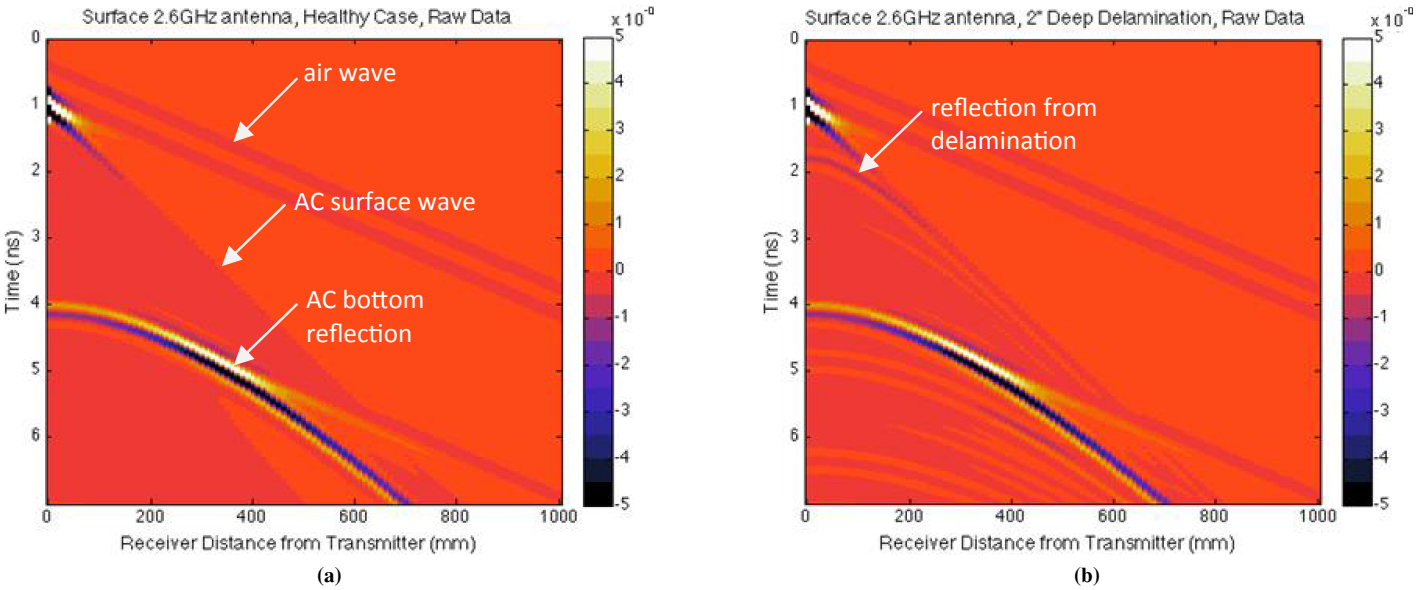

Figure 1.6. Move-out simulation results for (a) intact case and (b) delaminated at 2 in.

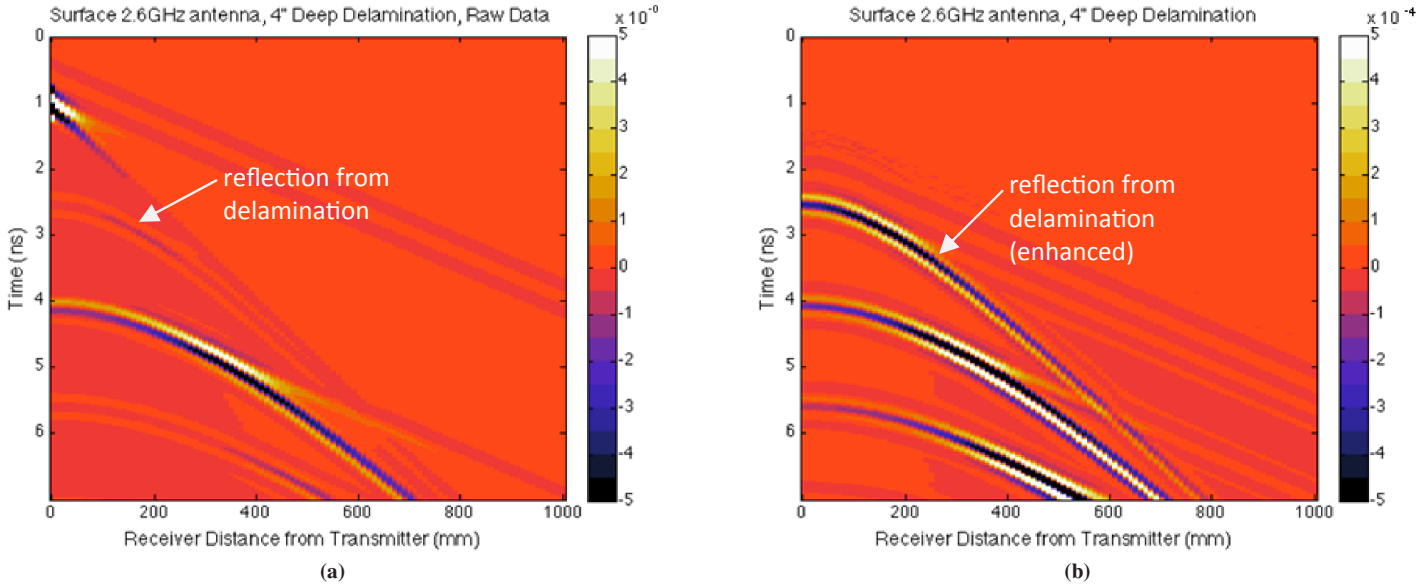

Figure 1.7. Move-out simulation results for (a) delamination at 4 in. and (b) delamination at 4 in. with intact results subtracted.

100 to 200 mm (3.9 to 7.9 in.) from the T and then decreases. This pattern suggested that there is an antenna spacing that optimizes the measured delamination response. In order to examine this effect in further detail, the reflection amplitude versus spacing is plotted in Figure 1.8. The figure shows that the optimum antenna spacing ranged from 100 to 170 mm (3.9 to 6.7 in.) for delamination depths ranging from 2 to 4 in.

Figure 1.9 shows the simulation results for the stripped asphalt layer between 3 and 4 in. The reflection from the stripped layer had two elements: the reflection from the top and the reflection from the bottom of the stripped layer.

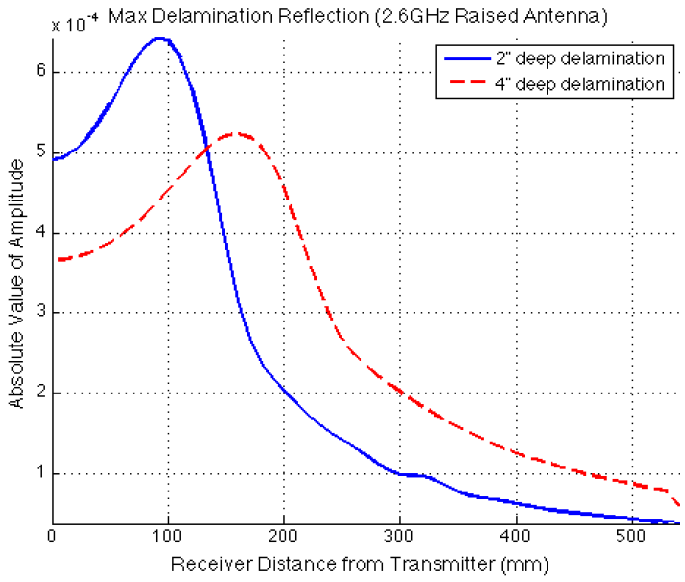

Figure 1.8. Amplitude versus move-out distance.

B-Scan Simulations

Sample B-scan simulation results are shown in Figure 1.10 for the intact, delamination, and stripped conditions. The results show that the delamination and stripping conditions are detectable in principle in the B-scan simulation model. Figures 1.10e and 1.10f show how the presence of moisture in the delamination significantly increased the response.

Conclusions from Electromagnetic Simulations

In all cases, the 2.6-GHz antenna provided better results than those of the 1.3-GHz antenna. Both frequencies provided adequate resolution down to the bottom of the deck (203 mm, or 8 in.). Changing the height of the T/R pair from zero to 3 mm (0.12 in.) above the surface seemed to have little impact on the results. As expected, water-filled delaminations were much more evident in the simulation results than were air-filled delaminations of the same size.

The move-out simulations showed that a T/R separation (as opposed to a monostatic configuration) was often desirable. However, the ideal separation was governed by a variety of factors, including depth of damage and the electromagnetic properties of the materials, both of which affected the angle of reflection. For this reason, an array configuration with a single T and multiple Rs may be beneficial. From the move-out results, it appears that spacing between 100 and 170 mm (3.9 and 6.7 in.) is optimal for detecting delaminations.

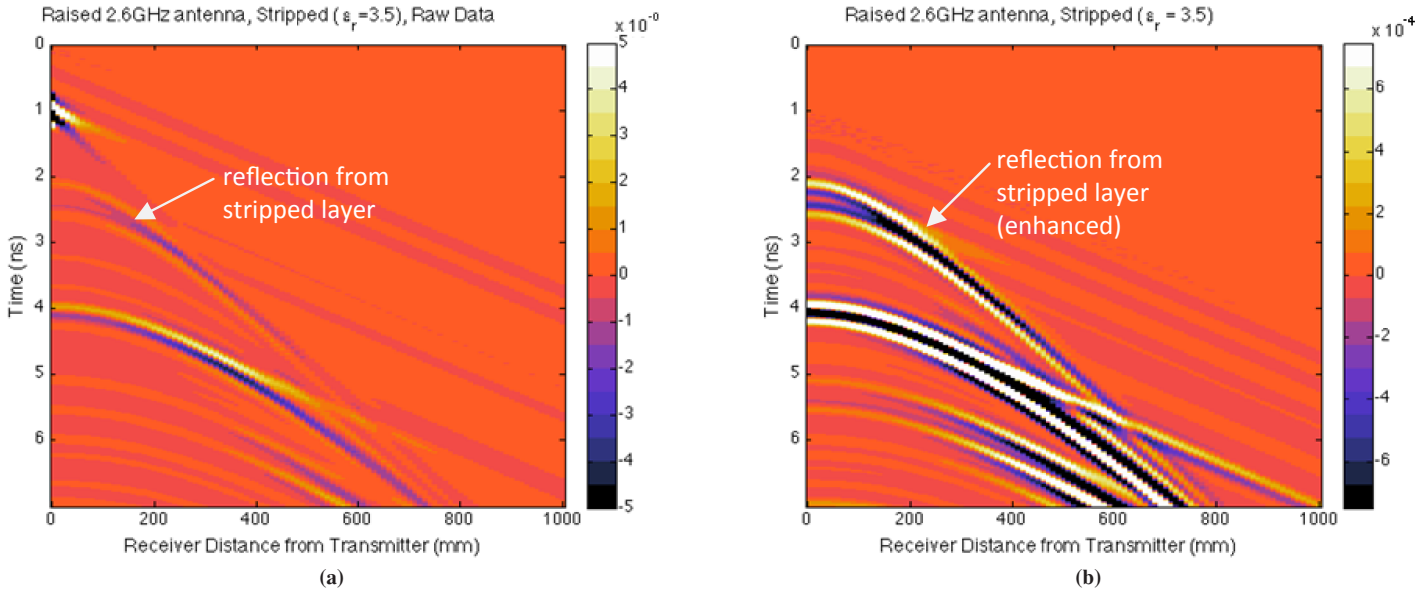

Figure 1.9. Move-out simulation results for (a) stripping (dry) between 3 and 4 in. and (b) stripping (dry) between 3 and 4 in. with intact results subtracted,

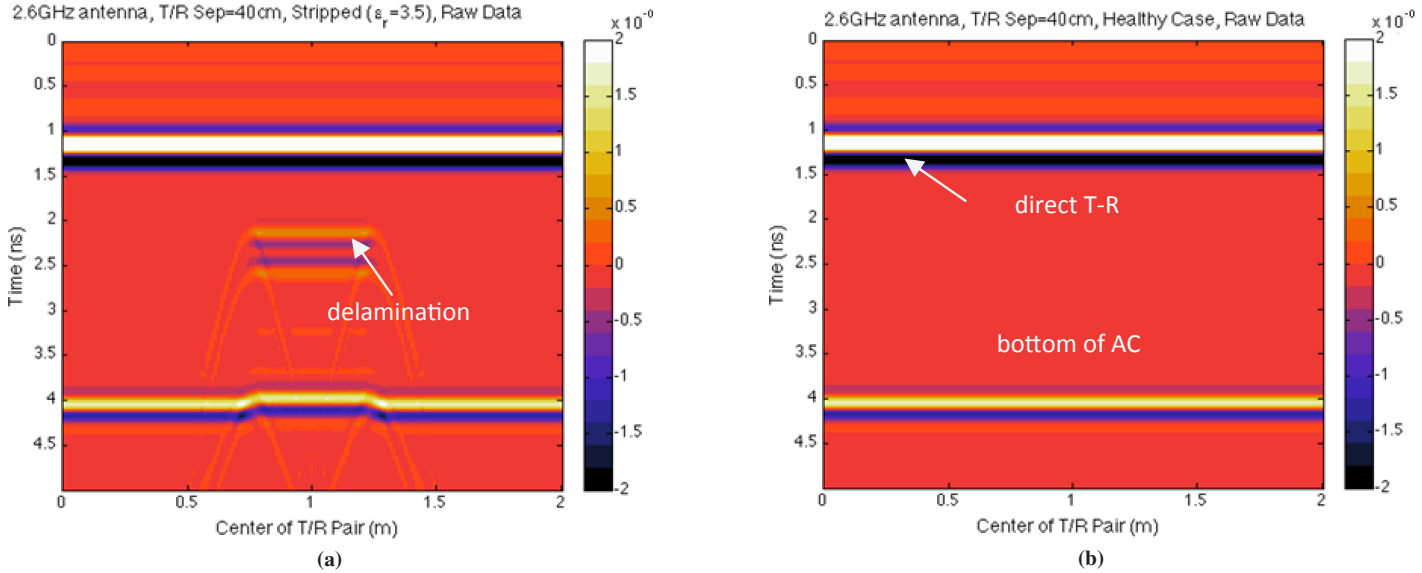

Figure 1.10. Sample B-scan simulation results for 2.6 GHz antenna model: (a) stripping (dry) at 3 to 4 in., (b) intact case.

(continued on next page)

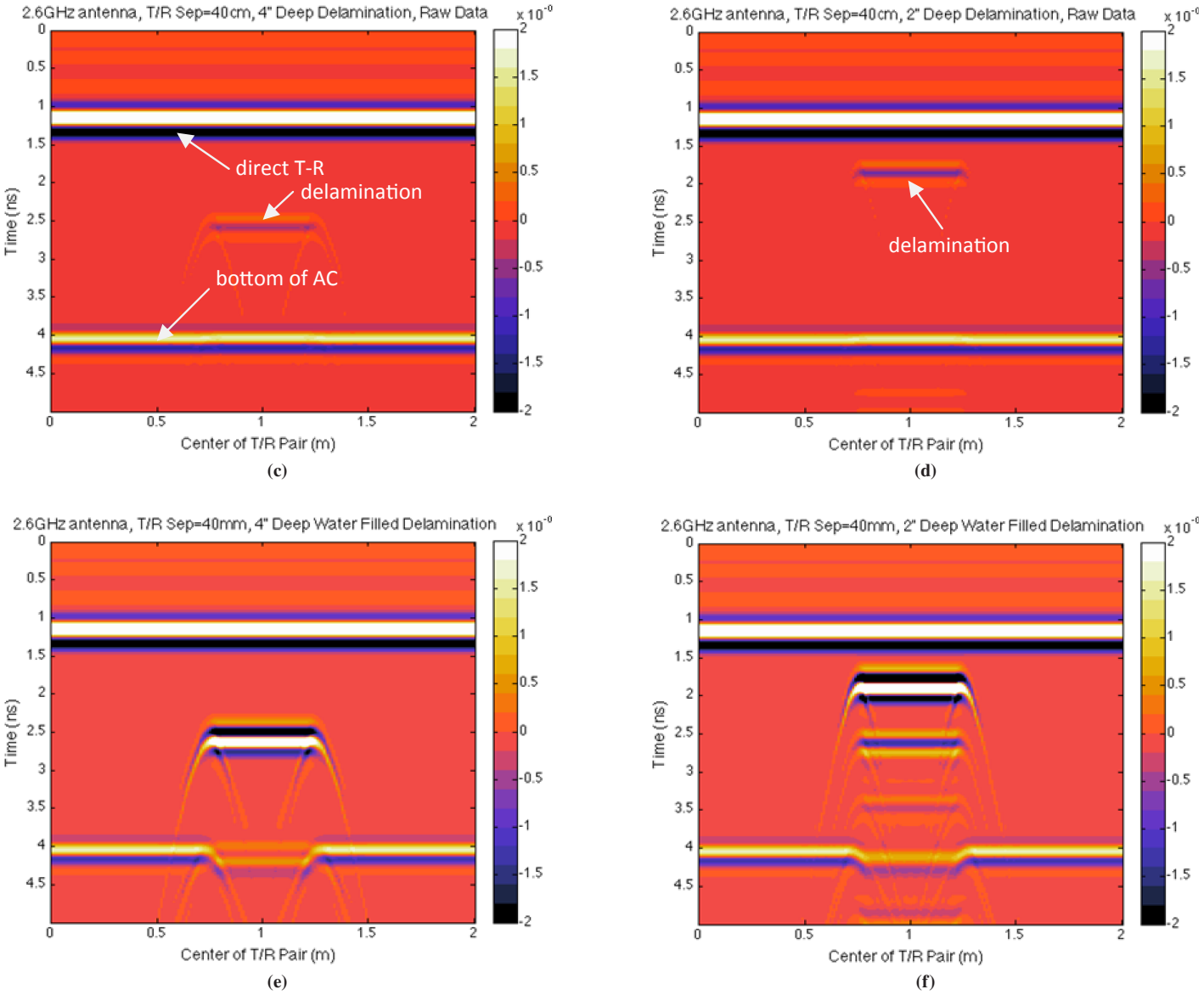

Figure 1.10. Sample B-scan simulation results for 2.6 GHz antenna model: (c) dry delamination at 4 in., (d) dry delamination at 2 in., (e) wet delamination at 4 in., and (f) wet delamination at 2 in. (continued).

CHAPTER 2

Theoretical Models for Infrared Thermography Technology

The numerical simulations presented in this chapter were carried out by Infrasense with support from Dr. Kim Belli of Northeastern University in Boston, Professor Dennis Hiltunen of the University of Florida, and Professor Rajib Mallick of Worcester Polytechnic Institute.

Numerical simulations of nondestructive testing (NDT) techniques were carried out to assess the NDT ability to detect delaminations and to evaluate the most promising configurations for implementing each NDT method. An NDT technique and/or configuration that does not show promise in the numerical simulations would not likely succeed in the field evaluations. Therefore, results obtained from the simulations would help the project team focus on the most promising methods or configurations, or both, in the laboratory and field evaluations.

The numerical simulations were conducted by using existing numerical models to simulate and compare simulation results of delaminated and intact pavements. The simulation information was used to define detectability and served to support recommendations of specific methods or configurations, or both, for the laboratory and field evaluations. Modeling provided insight into results that could be expected from laboratory and field experiments, and also offered guidance into the effective configurations of the transmitter and receiver for each NDT technique. Modeling results were considerably cleaner than were results obtained in the laboratory and field evaluations, and modeling results were based on certain idealizations of material characteristics and input signals. Simulation results showed (a) whether, under ideal conditions, the pavement defect could be detected; and (b) under what conditions detectability could be enhanced. For electromagnetic and mechanical wave methods, the simulation results could show how the relative placement of the source and receiver could affect the NDT detectability.

Model Description

The use of infrared (IR) thermography is based on the detection of surface thermal anomalies associated with subsurface defects. Those anomalies develop under the influence of solar heating and cooling. To evaluate the potential effectiveness of this method, thermal models were used to calculate the magnitude of surface thermal anomalies associated with delamination. The modeling was carried out by using the heat transfer module from COMSOL Multiphysics software. The basic model setup is shown in Figure 2.1.

Solar radiation is typically modeled as a parabolic input radiation pattern from sunrise to sunset, with radiational cooling and convection to ambient temperature taking place when there is no sunshine. For simplicity, the COMSOL model was used as a triangular input, as shown in Figure 2.2. Two types of solar inputs were considered. The first type was a continuous solar input assuming that the pavement was continuously exposed to the sun. The second type assumed that the solar input was blocked for a period of time after time t_b.

The other parameters used for the modeling effort were

- h = AC thickness = 200 mm;
- d = delamination depth = 50 mm;
- δ_s = thickness of stripped layer = 15 mm;
- δ_d = thickness of delamination = 1 mm;
- Qmax = 800, w/m^2;
- t_b = 11 a.m., 1 p.m., and 3 p.m.; and
- w = width of partial delamination = 60 mm.

The ambient temperature profile was 40°F (5°C used) from midnight to 6 a.m., increased linearly to 65°F (20°C used) from 6 a.m. to noon, decreased linearly to 40°F (5°C used) from noon to 6 p.m., and constant as 40°F (5°C used) from 6 p.m. to midnight. The thermal properties of the components in each model are shown in Table 2.1.

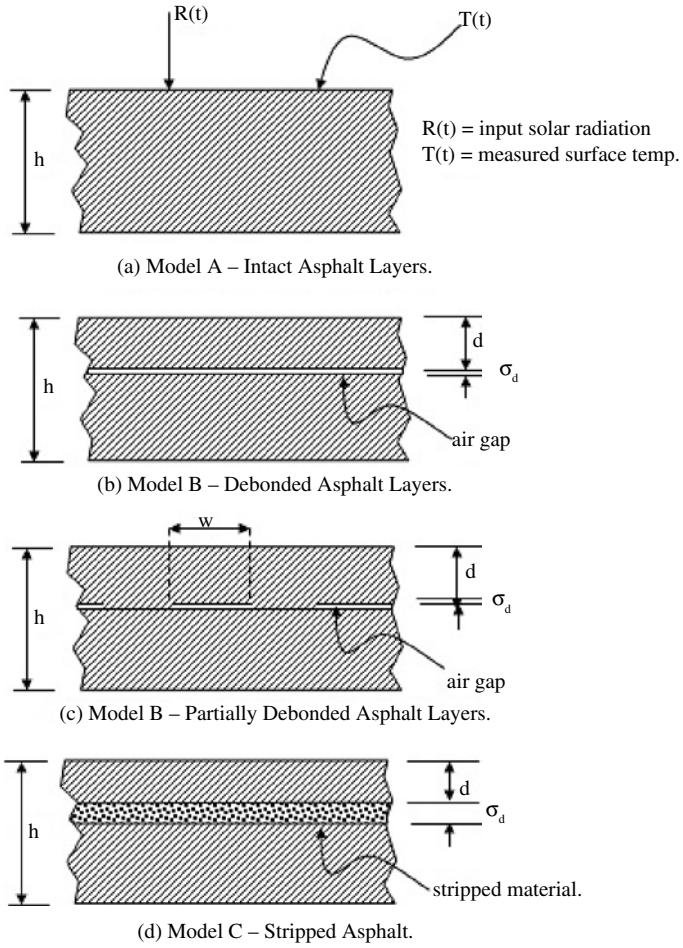

Figure 2.1. Structure of asphalt thermal models.

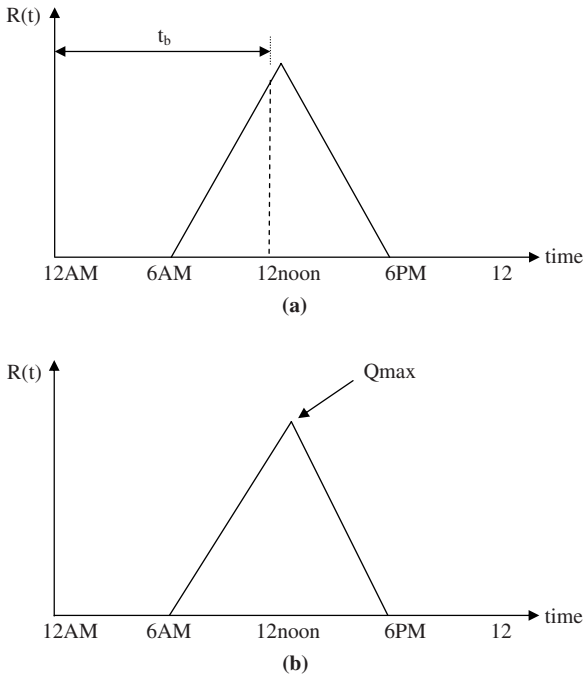

Figure 2.2. Solar radiation patterns: (a) solar input blocked after time t_b and (b) normal solar radiation.

Table 2.1. Thermal Properties of Components in Each Model

Component	Thermal Conductivity (W/m·K)	Heat Capacity (J/kg·K)	Density (kg/m³)
Intact asphalt	1	1,100	2,300
Stripped asphalt (1)	1	1,100	1,800
Stripped asphalt (2)	0.75	1,100	1,800
Stripped asphalt with 10% water	0.95	1,408	2,170
Air at 25°C	0.026	1,006.25	1.1843
Water at 25°C	0.6	4,186	1,000

The simulations carried out with the models were as follows:

- Model A, normal solar input;
- Model A, blocked solar input;
- Model B, wet and dry delamination;
- Model B, partial delamination;
- Model C, stripped asphalt, $k = 1.0$; and
- Model C, same as Model C above, with k of stripped material = 0.75.

Discussion of Results

Sample results of these simulations are shown in Figures 2.3 through 2.5. The results in each figure show the temperature differential, which is the temperature response for each condition minus the temperature response for the intact condition (Model A).

A typical commercial IR camera used for capturing images of asphalt pavements can distinguish temperature differentials on the order of 1°C. On the basis of results shown in Figure 2.3, it appeared that the temperature differentials produced by a dry stripped pavement layer were below the threshold of detectability. On the other hand, the results in Figure 2.4 for the air-filled delamination showed temperature differentials of up to 3°C, which were within the detectable range. In Figure 2.5, the model represented a delaminated layer interface with partial contact and smaller air gaps. Using this representation, the maximum temperature differential decreased by half, and the likelihood of detection was reduced. Unlike with GPR, introducing moisture into the delamination or stripped area reduced the likelihood of detection.

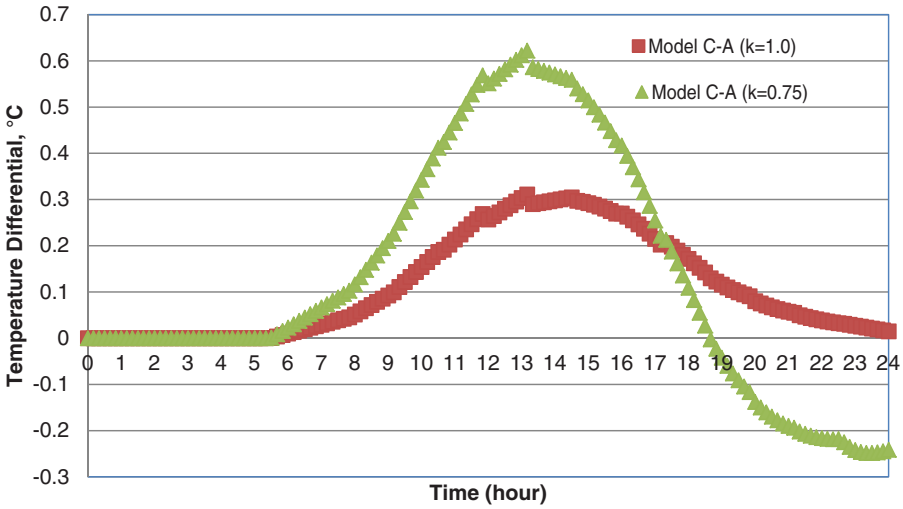

Figure 2.3. Results for dry stripped layer.

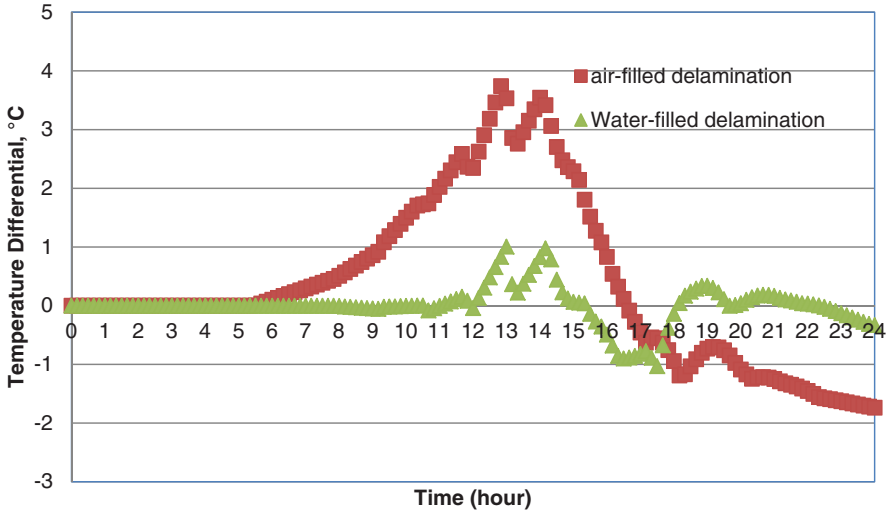

Figure 2.4. Results for air- and water-filled delamination.

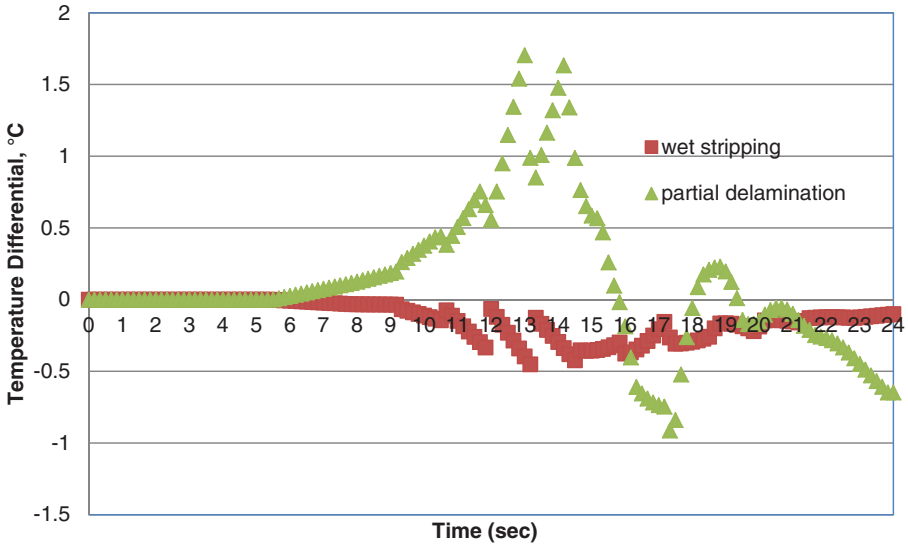

Figure 2.5. Results for partial delamination and wet stripped layer.

CHAPTER 3

Theoretical Models for Mechanical Wave Technology: Impact Echo, Impulse Response, and Ultrasonic Surface Waves

The numerical simulations presented in this chapter were carried out by Infrasense with support from Dr. Kim Belli of Northeastern University in Boston, Professor Dennis Hiltunen of the University of Florida, and Professor Rajib Mallick of Worcester Polytechnic Institute.

Numerical simulations of nondestructive testing (NDT) techniques were carried out to assess the NDT ability to detect delaminations and to evaluate the most promising configurations for implementing each NDT method. An NDT technique and/or configuration that does not show promise in the numerical simulations would not likely succeed in the field evaluations; therefore, results obtained from the simulations would help the project team focus on the most promising methods or configurations, or both, in the laboratory and field evaluations.

The numerical simulations were conducted by using existing numerical models to simulate and compare simulation results of delaminated and intact pavements. The simulation information was used to define detectability and served to support recommendations of specific methods or configurations, or both, for the laboratory and field evaluations. Modeling provided insight into results that could be expected from laboratory and field experiments, and also offered guidance into the effective configurations of the transmitter and receiver for each NDT technique. Modeling results were considerably cleaner than were results obtained in the laboratory and field evaluations, and modeling results were based on certain idealizations of material characteristics and input signals. Simulation results showed (a) whether, under ideal conditions, the pavement defect could be detected; and (b) under what conditions detectability could be enhanced. For electromagnetic and mechanical wave methods, the simulation results could show how the relative placement of the source and receiver could affect the NDT detectability.

Introduction

This study explores the possibilities of using mechanical waves to detect flexible pavement with delamination. When finite element software was used, the behavior of sound pavement was evaluated and a parametric study on delaminated pavement was then elaborated. By comparing the differences in dispersion images, the parametric study shows how the impacts of different variables are related to the properties of the pavement with delamination.

Previous Work

Munoz (2009) conducted an extensive evaluation of capabilities of mechanical wave testing methods to characterize pavements containing delaminations. The evaluation used finite element simulations, and included impact echo (IE), impulse response, and ultrasonic surface waves (USW) methodologies. An overview of this study is provided in the following sections.

Finite Element Model

Important features of the finite element models used in the work were as follows:

- The finite element analysis was conducted with the commercial software LS-DYNA 3D.
- For USW and IE methodologies, the pavement model was $0.5 \times 0.5 \times 0.5$ m in size and used $10 \times 10 \times 10$ mm 8-node solid elements.
- For the impulse response methodology, the pavement model was $2 \times 2 \times 0.5$ m in size and used $25 \times 25 \times 25$ mm 8-node solid elements.
- The pavement models contained seven layers: four 50-mm layers for the hot-mix asphalt (HMA), two 100-mm layers

for the base, and one 100-mm layer for the subgrade, for a total depth of 0.5 m.
- Nonreflecting boundaries were used to absorb energy.
- An impact source was modeled with a half-sine curve with duration of 52.5 μs for the USW and IE methodologies, and 0.2 ms for the impulse response methodology.

Parameters

Six parameters of the pavement models were investigated with the finite element simulations. The parameters were

- Degree of defect = bonded, partially debonded, and totally debonded interface conditions;
- Depth of defect = 50, 100, and 150 mm from surface;
- Size of defect = 100 × 100 mm, 300 × 300 mm, and 500 × 500 mm in horizontal extent;
- HMA modulus = 12.5, 8.3, 6.25, and 4.2 GPa;
- Base modulus = 1,250, 700, and 315 MPa; and
- HMA thickness = 200, 150, and 100 mm.

Impact Echo

The IE methodology was investigated by using a standard one-impact source and one-receiver configuration. The significant findings were as follows:

- Degree of defect: totally and partially debonded defects were detectable and accurately located in frequency domain (Figure 3.1).
- Defect depth: totally debonded defects were detectable and accurately located in frequency domain for depths of 100 and 150 mm; for 50 mm, the method generated a dominant flexural mode (Figure 3.2).
- Defect size: totally debonded defects were detectable and accurately located in frequency domain for 300 × 300 mm and 500 × 500 mm defects; for 100 × 100 mm, the dominant frequency was near the thickness of HMA (some diffraction effect due to defect), while the defect was correctly located via a smaller peak (Figure 3.3).
- HMA modulus: totally debonded defects were detectable and accurately located in frequency domain, but the HMA modulus needed to be known for accurately locating the defect (Figure 3.4).
- Base modulus: totally debonded defects were detectable and accurately located in frequency domain independent of base modulus (Figure 3.5).
- HMA thickness: totally debonded defects were detectable and accurately located in frequency domain independent of HMA thickness for a given defect location (Figure 3.6).

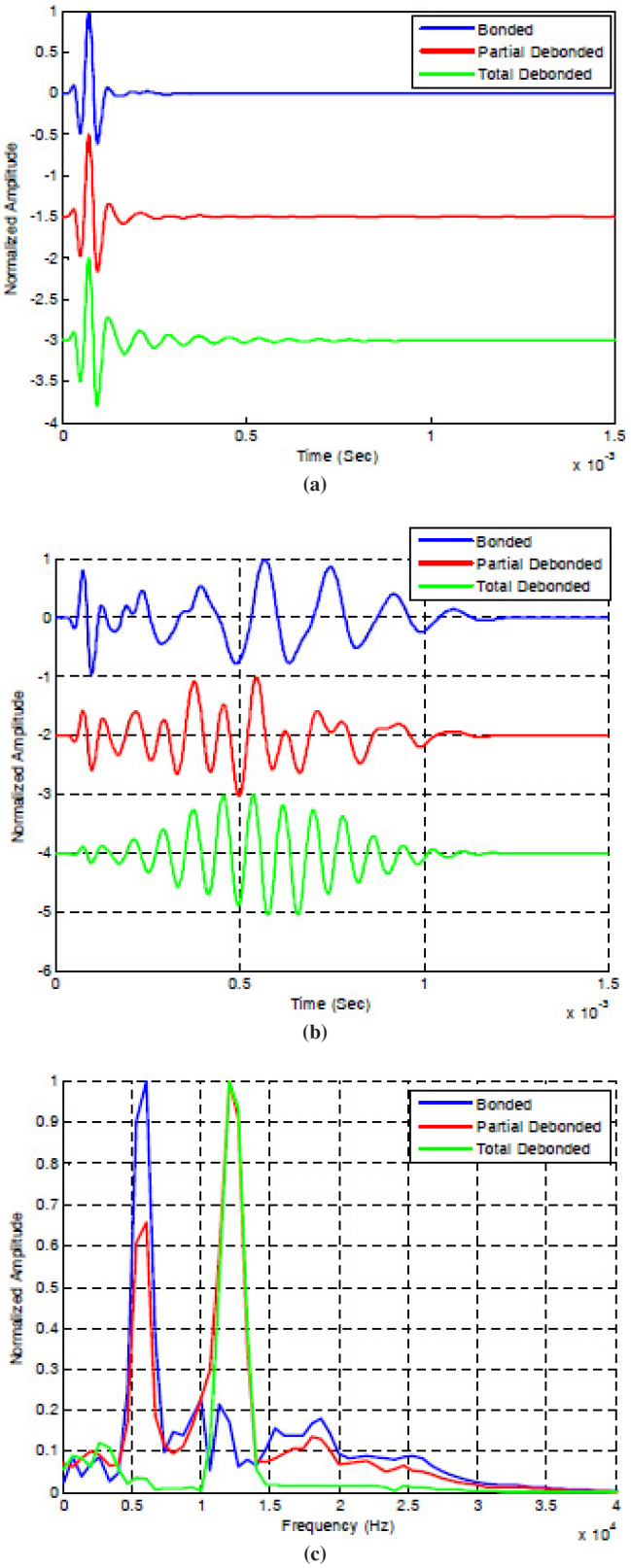

Source: Munoz 2009.

Figure 3.1. Degree of defect: (a) time record signals, (b) time record after applying the Blackman-Harris window, and (c) frequency spectra of signals.

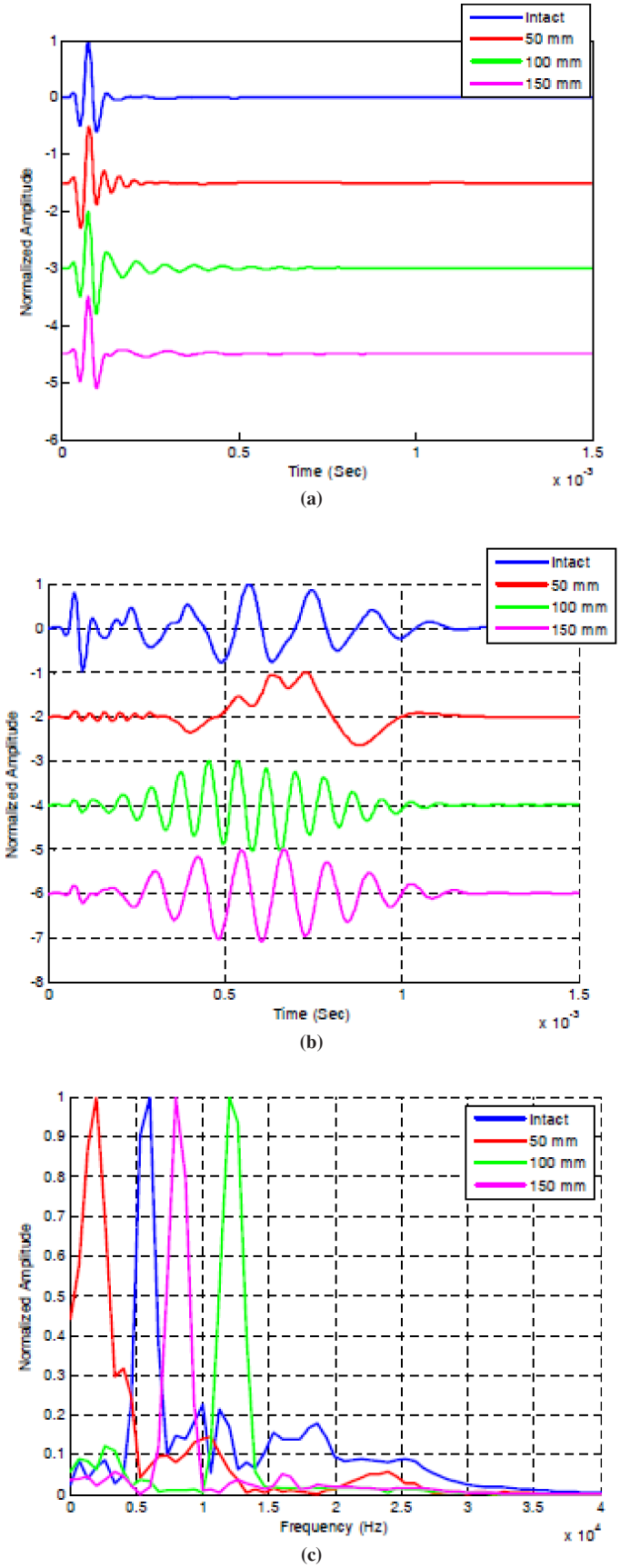

Source: Munoz 2009.

Figure 3.2. Defect depth: (a) time record signals, (b) time record after applying the Blackman-Harris window, and (c) frequency spectra of signals.

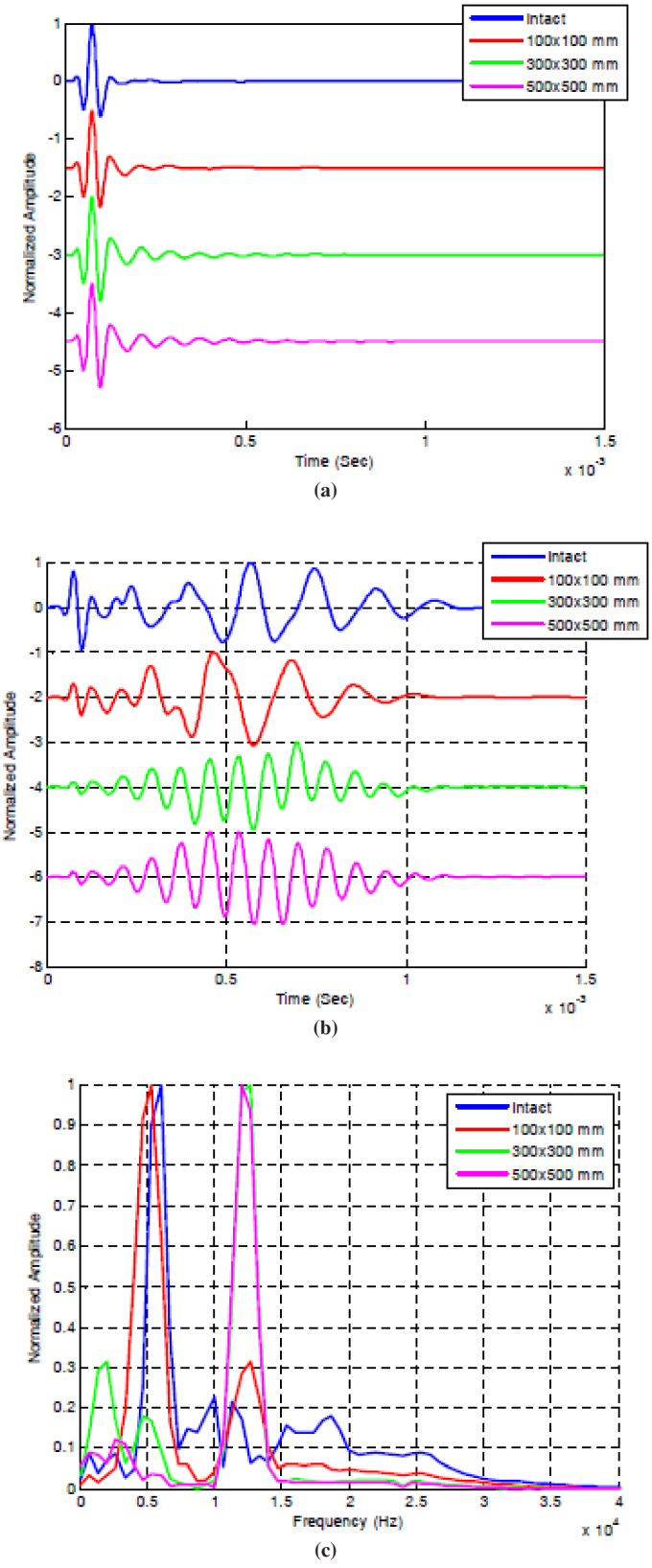

Source: Munoz 2009.

Figure 3.3. Defect size: (a) time record signals, (b) time record after applying the Blackman-Harris window, and (c) frequency spectra of signals.

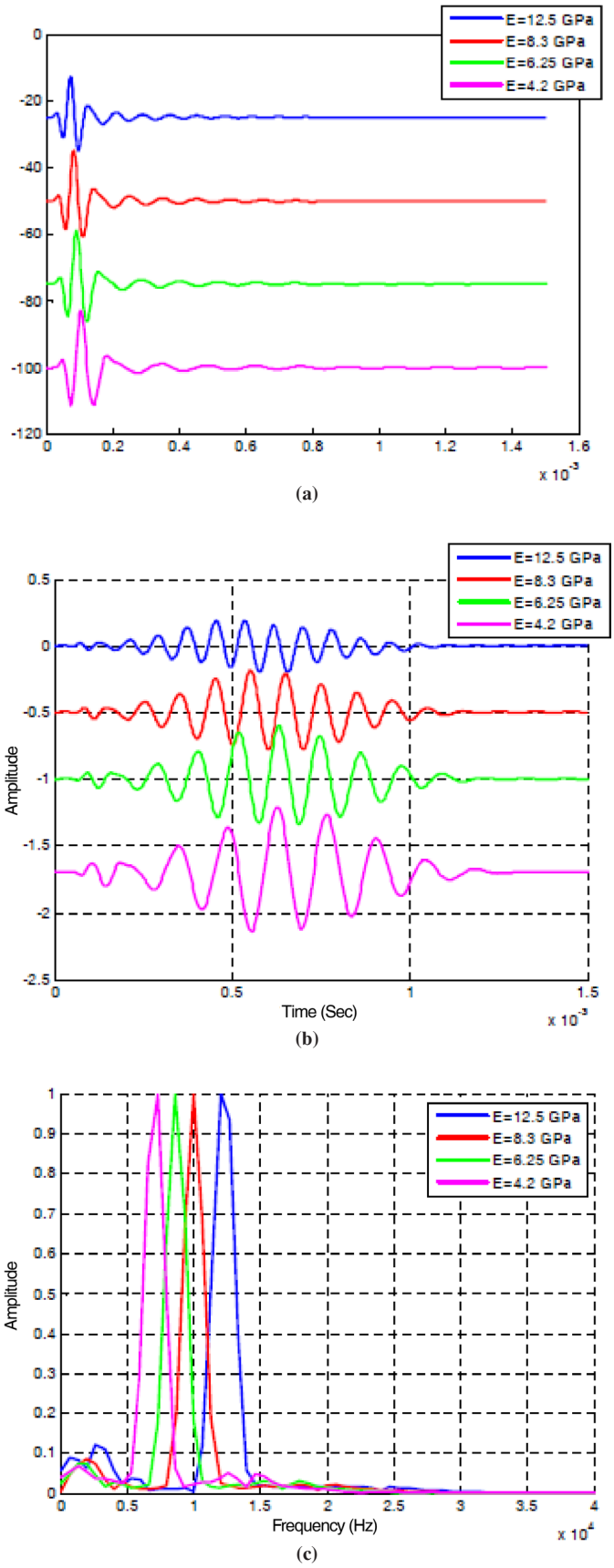

Source: Munoz 2009.

Figure 3.4. HMA modulus: (a) time record signals, (b) time record after applying the Blackman-Harris window, and (c) frequency spectra of signals.

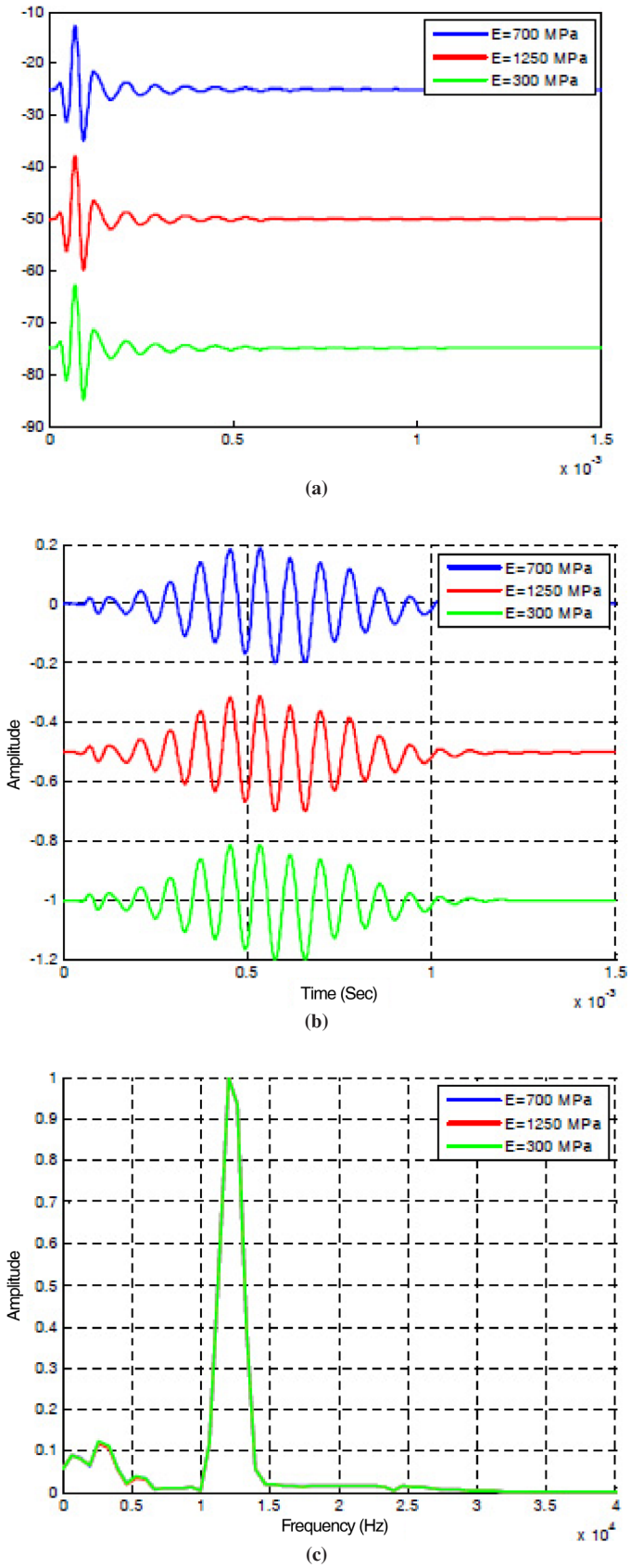

Source: Munoz 2009.

Figure 3.5. Base modulus: (a) time record signals, (b) time record after applying the Blackman-Harris window, and (c) frequency spectra of signals.

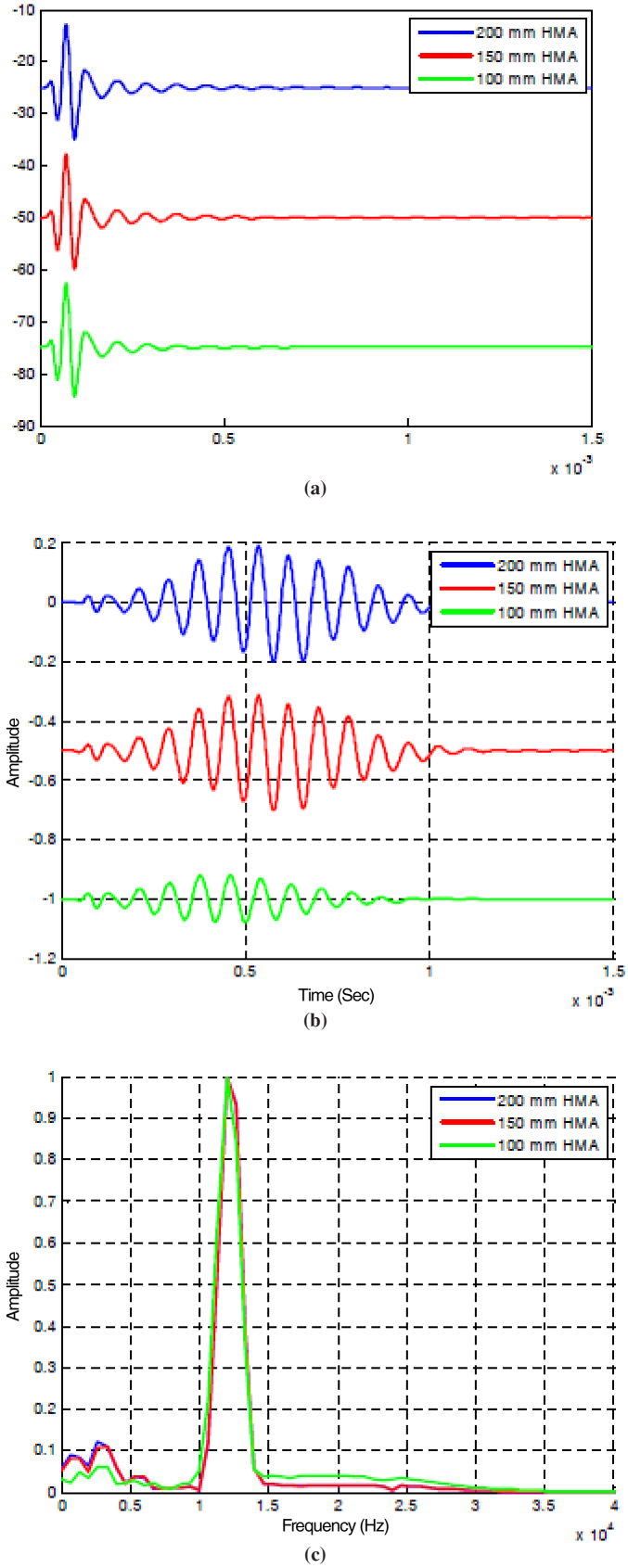

Source: Munoz 2009.

Figure 3.6. HMA thickness: (a) time record signals, (b) time record after applying the Blackman-Harris window, and (c) frequency spectra of signals.

Impulse Response

The impulse response methodology was investigated by using a standard one-impact source and one-receiver configuration. The significant findings were as follows:

- Degree of defect: totally and partially debonded defects could be differentiated from the intact response (Figure 3.7).
- Defect depth: totally debonded defects could be differentiated from intact response for depths of 50 and 100 mm; for 150 mm, the response with defect was similar to intact response (Figure 3.8).
- Defect size: totally debonded defects could be differentiated from intact response for defect sizes of 500 × 500 mm; for 300 × 300 mm and 100 × 100 mm, the responses with defect were similar to intact response (Figure 3.9).
- HMA modulus: totally debonded defects could be differentiated from intact response, but response was dependent on HMA modulus (Figure 3.10).
- Base modulus: totally debonded defect response was independent of base modulus (Figure 3.11).

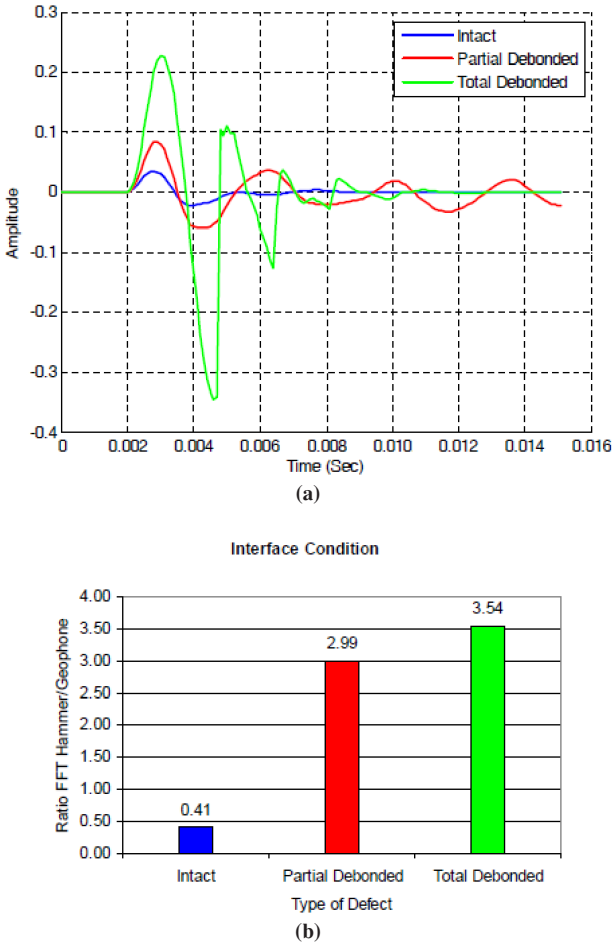

Source: Munoz 2009.

Figure 3.7. Degree of defect: (a) signal from geophone and (b) Fast Fourier Transform (FFT) hammer/geophone.

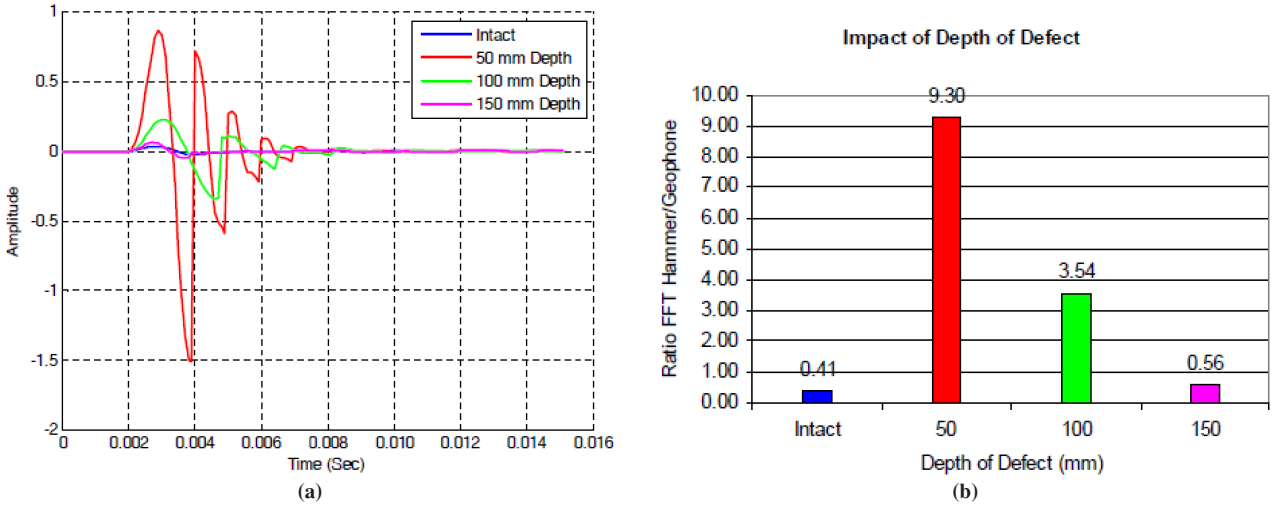

Source: Munoz 2009.

Figure 3.8. Defect depth: (a) signal from geophone and (b) FFT hammer/geophone.

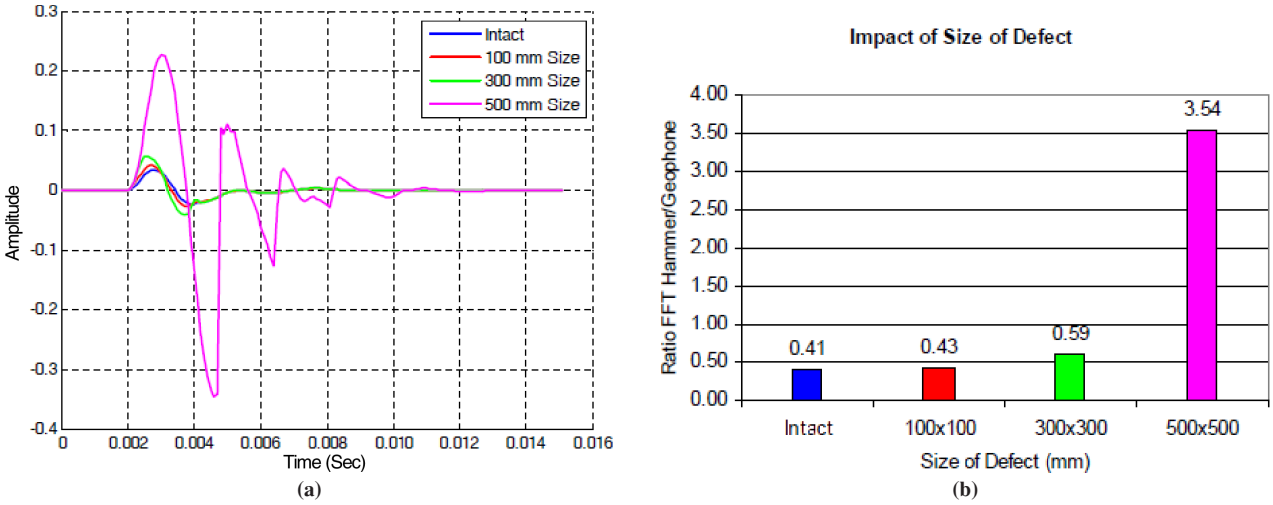

Source: Munoz 2009.

Figure 3.9. Defect size: (a) signal from geophone and (b) FFT hammer/geophone.

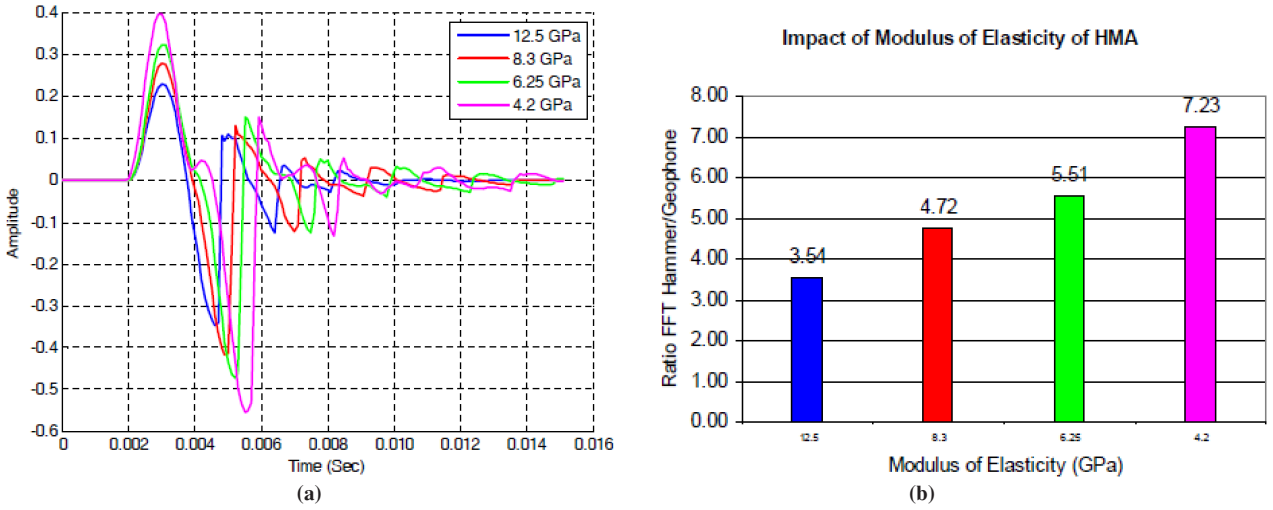

Source: Munoz 2009.

Figure 3.10. HMA modulus: (a) signal from geophone and (b) FFT hammer/geophone.

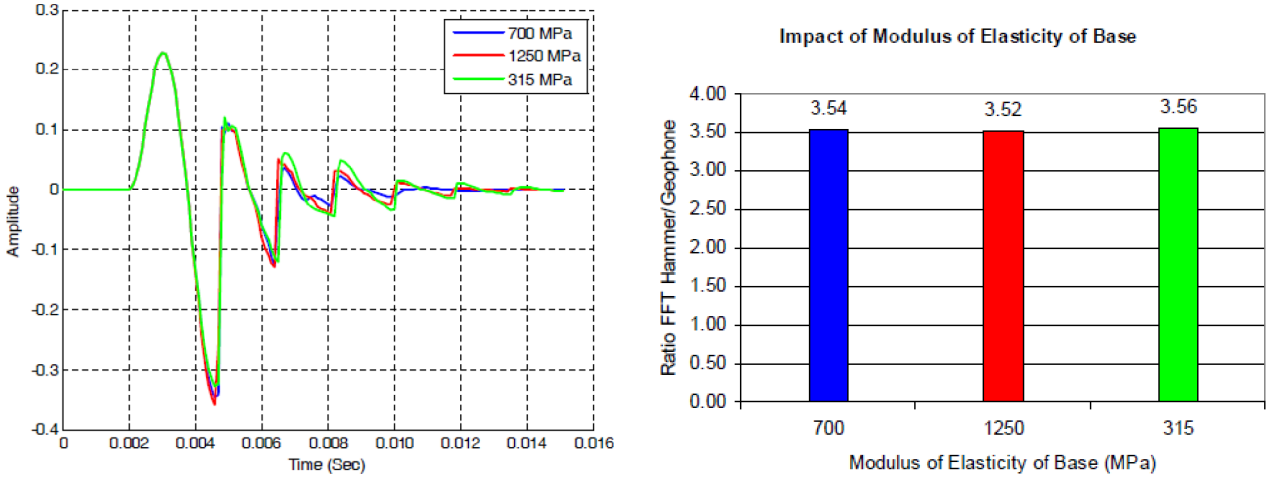

Source: Munoz 2009.

Figure 3.11. Base modulus: (a) signal from geophone and (b) FFT hammer/geophone.

- HMA thickness: totally debonded defect responses were similar for thicknesses of 150 and 200 mm; the response was smaller for 100 mm (Figure 3.12).

Ultrasonic Surface Waves

The USW methodology was investigated by using a standard configuration of one impact source and two receivers, and was intended to simulate a PSPA test device. The significant findings were as follows:

- Degree of defect: totally debonded defects could be differentiated from intact response; the response was similar to intact for partially debonded defects (Figure 3.13).
- Defect depth: totally debonded defects could be differentiated from intact response for depths of 50 and 100 mm; the response was similar to intact response for 150 mm (Figure 3.14).
- Defect size: totally debonded defects could be differentiated from intact response for defect sizes of 500 × 500 mm and 300 × 300 mm; the response was similar to intact response for 100 × 100 mm (Figure 3.15).
- HMA modulus: totally debonded defects could be differentiated from intact response, but response was dependent on HMA modulus (Figure 3.16).
- Base modulus: the response from totally debonded defects was independent of base modulus (Figure 3.17).
- HMA thickness: the response for totally debonded defects was similar for thicknesses of 150 and 200 mm, but slightly different for a thickness of 100 mm (Figure 3.18).

(text continued on page 25)

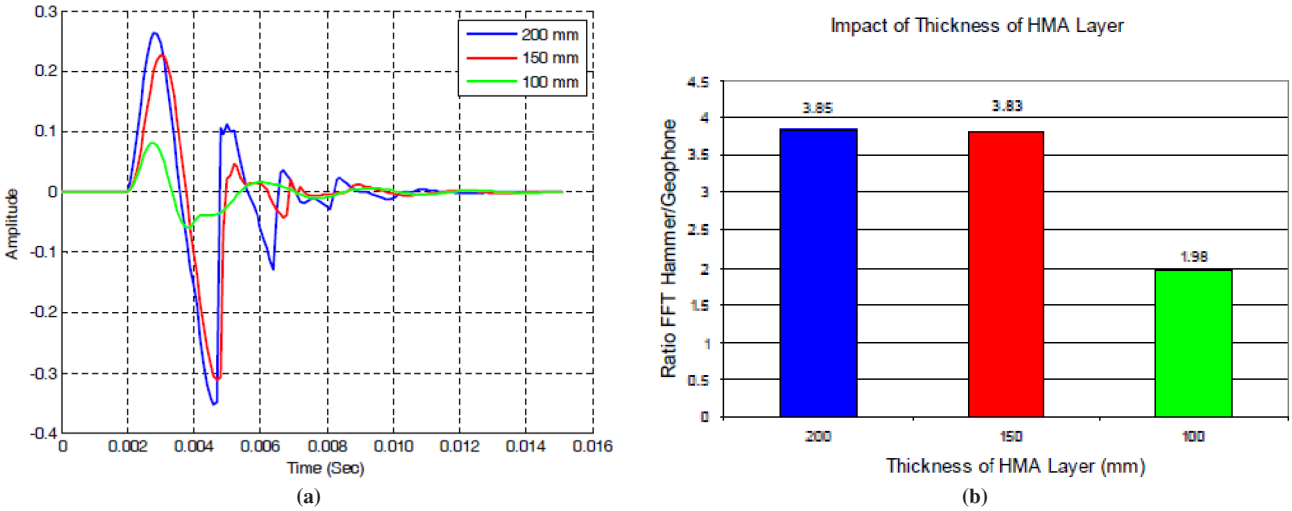

Source: Munoz 2009.

Figure 3.12. HMA thickness: (a) signal from geophone and (b) FFT hammer/geophone.

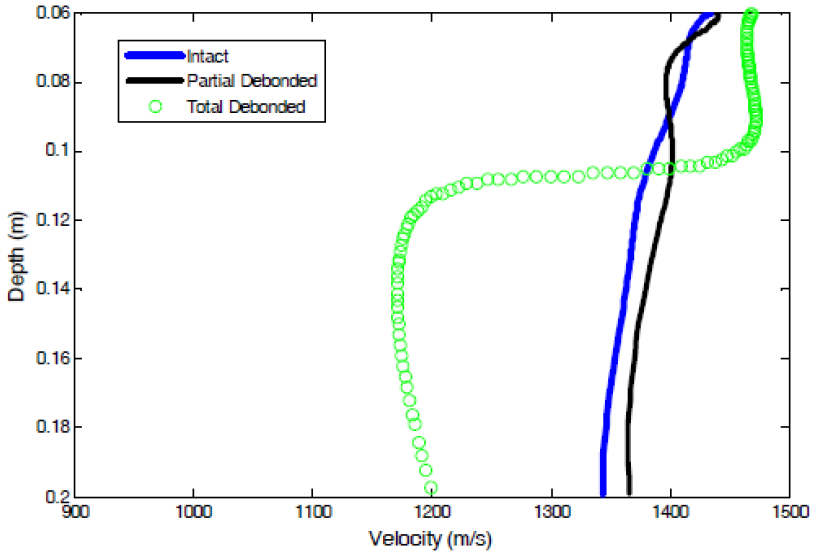

(a)

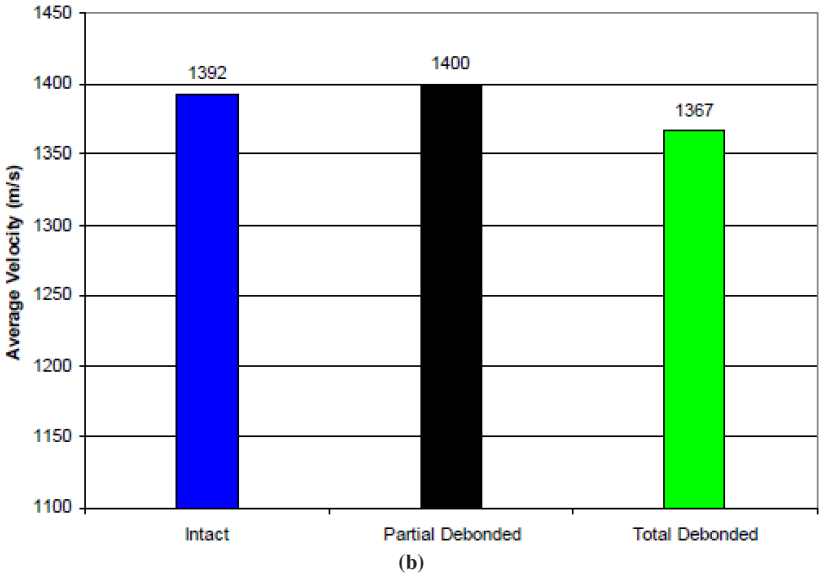

(b)

Source: Munoz 2009.

Figure 3.13. Degree of defect: (a) dispersion curves and (b) average velocity of surface waves.

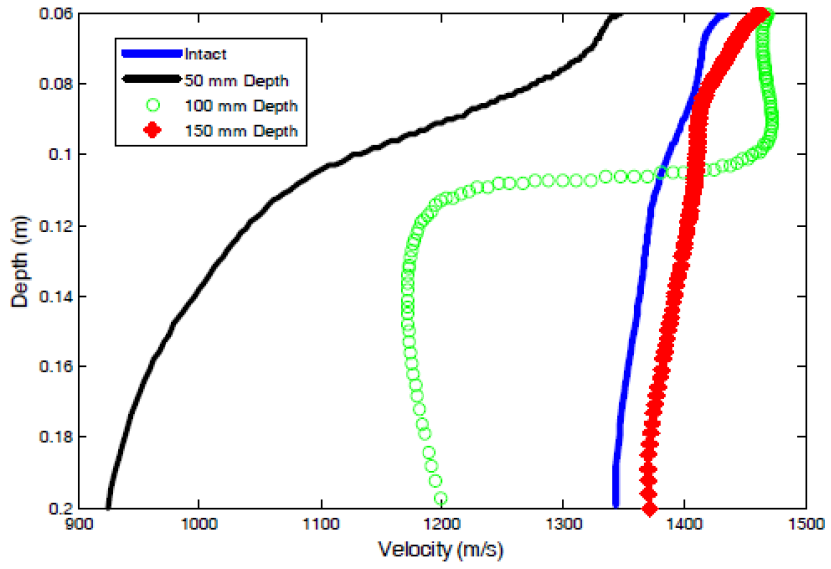

(a)

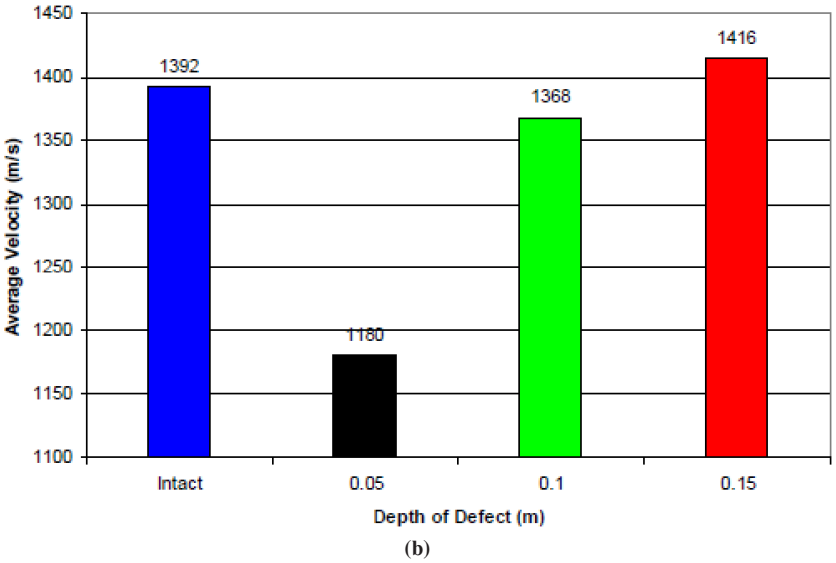

(b)

Source: Munoz 2009.

Figure 3.14. Defect depth: (a) dispersion curves and (b) average velocity of surface waves.

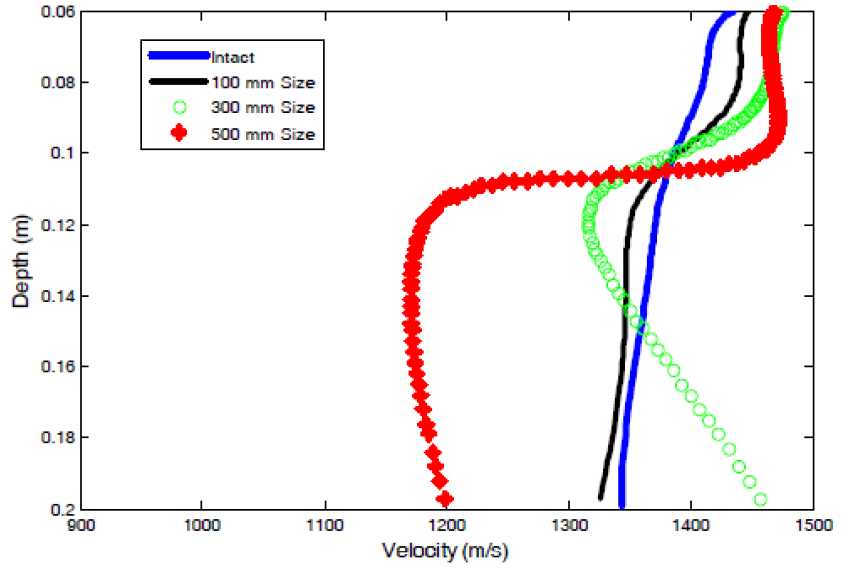

(a)

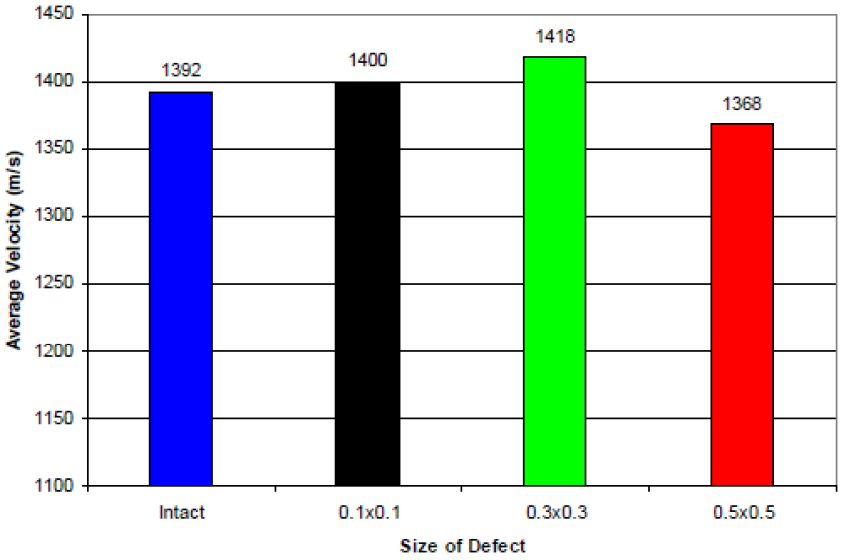

(b)

Source: Munoz 2009.

Figure 3.15. Defect size: (a) dispersion curves and (b) average velocity of surface waves.

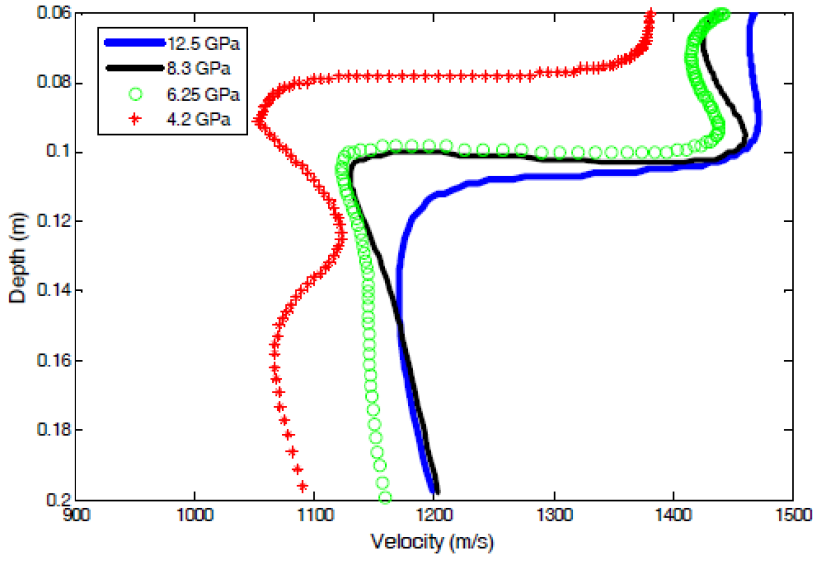

(a)

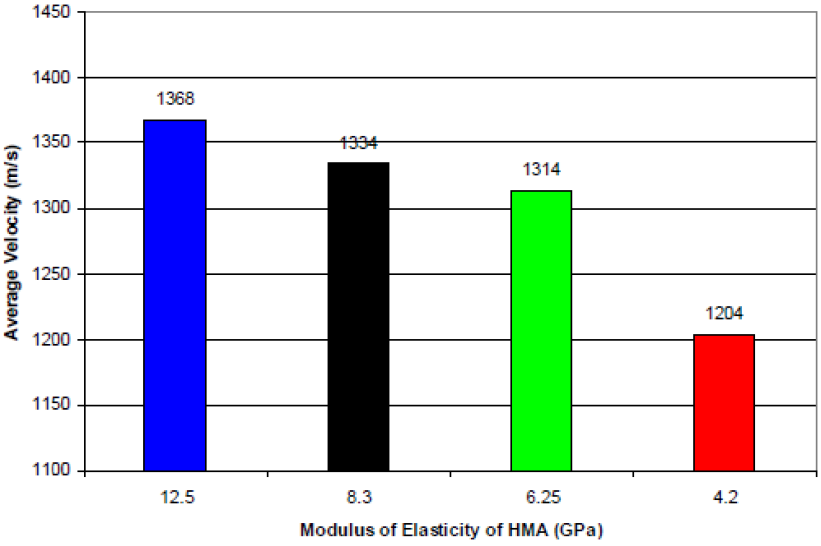

(b)

Source: Munoz 2009.

Figure 3.16. HMA modulus: (a) dispersion curves and (b) average velocity of surface waves.

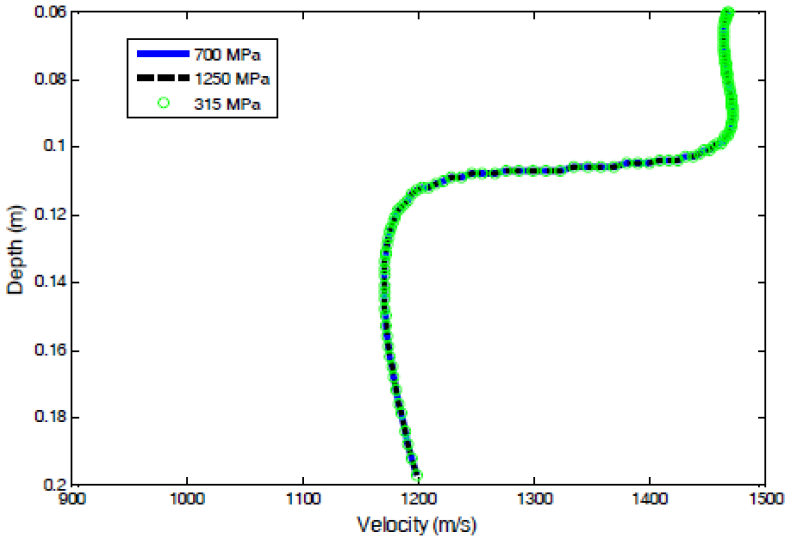

(a)

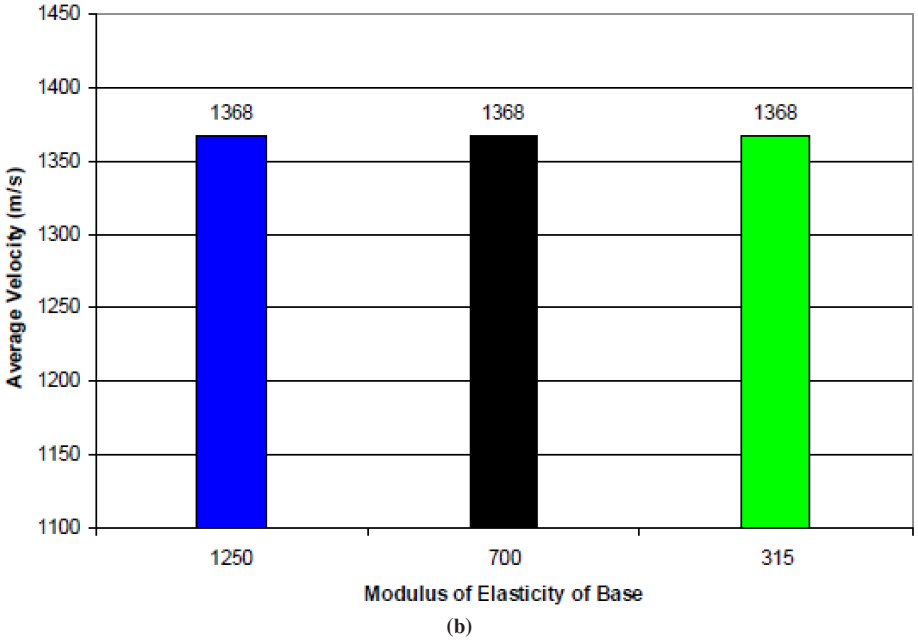

(b)

Source: Munoz 2009.

Figure 3.17. Base modulus: (a) dispersion curves and (b) average velocity of surface waves.

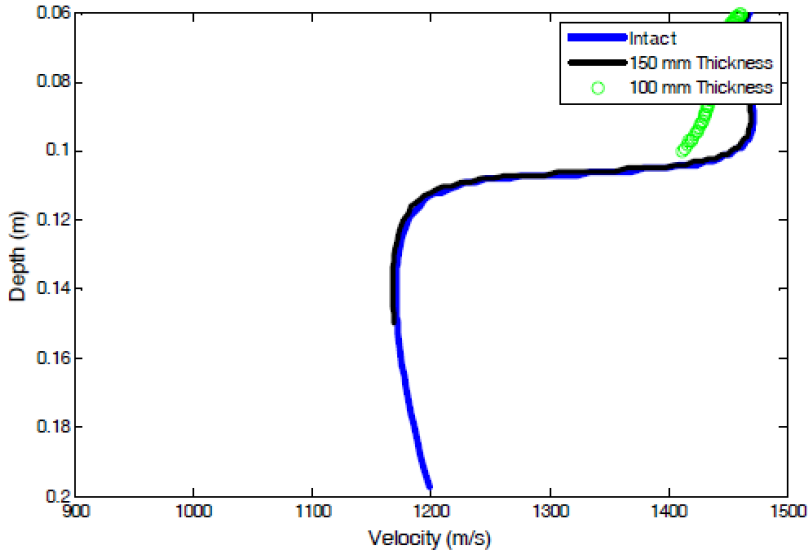

(a)

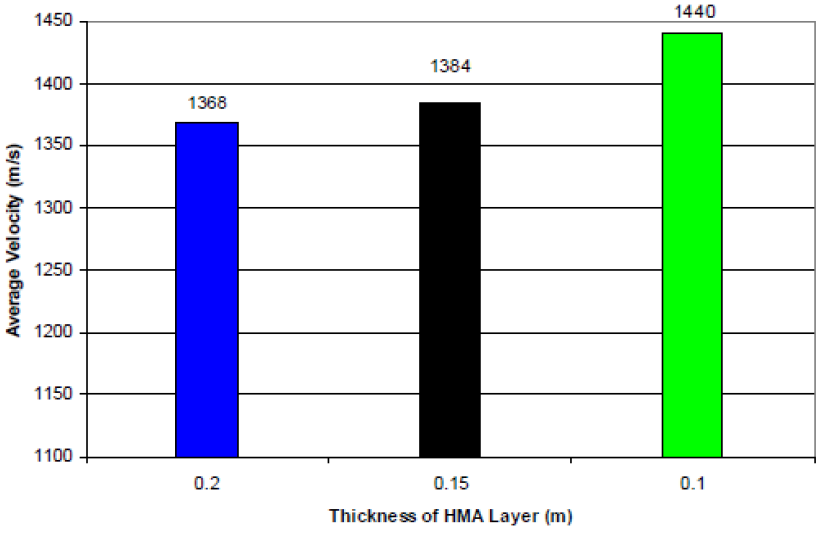

(b)

Source: Munoz 2009.

Figure 3.18. HMA thickness: (a) dispersion curves and (b) average velocity of surface waves.

Numerical Modeling

As reviewed in the previous sections, Munoz (2009) has demonstrated the significant capability of mechanical wave methods to characterize pavements with delaminations. One of the serious limitations revealed in the study was the inability of PSPA-based (two-sensor) ultrasonic surface waves to distinguish partial debonding. Therefore, further finite element simulations were conducted to investigate whether multiple-sensor surface wave techniques could provide better characterization of defects. Multiple-sensor techniques have been widely implemented in geotechnical site investigations in recent years because of the improved resolution that can be achieved. The multiple-sensor techniques also provide a more fundamental understanding of the characteristics of the wave field, and it was anticipated that this advanced understanding could further resolve delamination defects in pavements.

Delamination is generally known as a weak bonding between adjacent HMA layers, producing a sliding effect between layers and thus creating flaws such as slippage and potholes at later stages. In this study, the delaminations were modeled with two approaches: (1) a very thin layer (2-mm thick) with low modulus and (2) an interface element introduced between HMA lifts.

For the numerical study, a number of criteria have been taken into account to ensure accuracy of the results. The criteria considered were the dimensions of model, element size, sampling rate, impact frequency, and total time of recording, as follows:

- Axisymmetric models were used to simulate three-dimensional (3-D) wave propagation in reality, with dimensions 2 m wide by 1 m deep (Figure 3.19).
- 15-node triangular elements were used with an effective element length of 1 cm.
- The energy was created via a vertical impact source modeled as a triangular time pulse with duration of either 100 μs (10 kHz) or 50 μs (20 kHz), and was located at the upper left corner of the model (Figure 3.19).
- The output time histories from the PLAXIS model were in terms of vertical particle velocities collected along the top HMA surface via a linear, nonuniform array at 20 locations (Figure 3.20). This array was intended to simulate real data collection in a multichannel analysis of surface waves (MASW) test by using geophone velocity transducers on a pavement specimen. As done in the field, the array has been optimized to produce a high-quality dispersion image. The dense sensors at the beginning were to ensure high frequency resolution, while the array length of 0.6 m was to ensure that surface waves with long wavelengths (low frequencies) were included in the collected signals. Also note that the initial 0.5-m offset of the source from the first receiver was to reduce the so-called near-field effect at low frequencies.
- The sampling rate for the output time histories was chosen to be 0.1 μs, and the total record length was 10 ms.
- As shown in Figure 3.19, the model was divided into several different layers from top to bottom: three layers with a thickness of 5 cm each for the HMA layers, one layer with a thickness of 25 cm to represent the base, and one layer with a thickness of 0.60 m for the subgrade, for a total depth of 1 m.
- As indicated in Figure 3.19 via the PLAXIS symbols, the left and right boundaries were fixed from horizontal translation but were allowed to move vertically, while the bottom boundary was fixed from both horizontal and vertical translation.

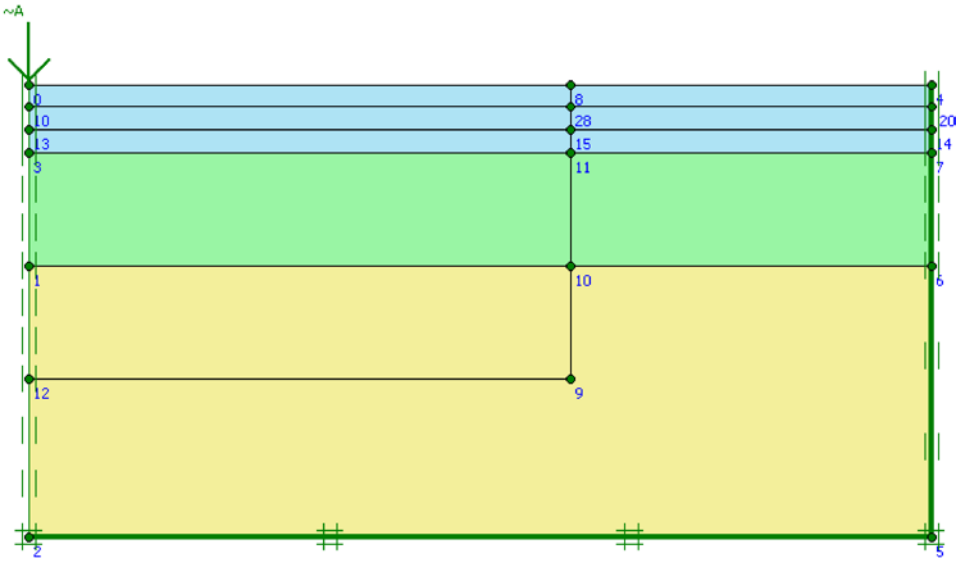

Figure 3.19. Pavement model layout.

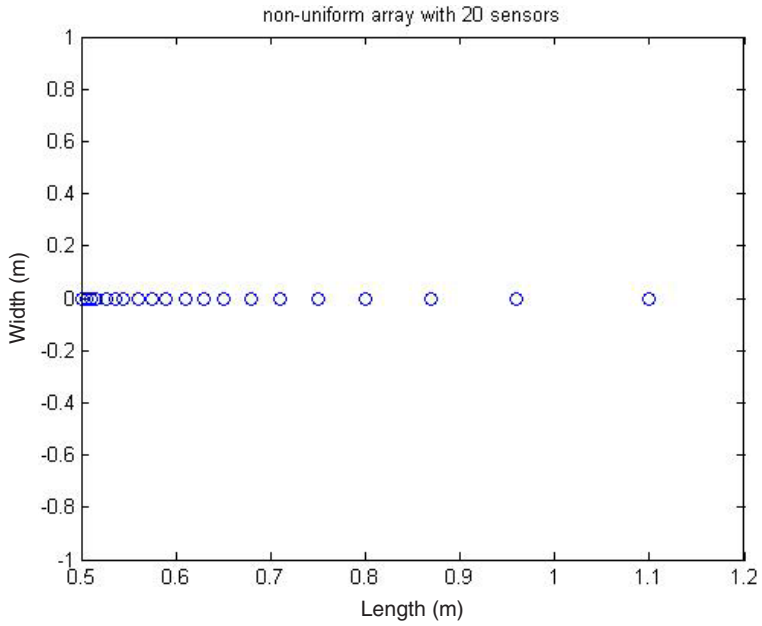

Figure 3.20. Nonuniform array.

- Absorbing boundaries were applied along the bottom and right edges to simulate the continuity of the materials, thus eliminating reflecting waves bouncing back from the boundaries.

Parametric Study

The parametric study was conducted by using a control model as described above and having material properties as indicated in Table 3.1. The effects of the parameters shown in Table 3.2 were then systematically investigated, as follows:

- Three defect depths of 5, 10, and 15 cm were investigated for an HMA layer with $V_s = 888$ m/s (control).
- Three HMA stiffnesses having shear wave velocities of $V_s = 400$, $V_s = 888$, and $V_s = 1{,}250$ m/s were investigated for a defect at 5 cm depth.
- The delamination was modeled in two ways: a soft, thin layer and an interface element; the severity of the delamination was investigated with HMA $V_s = 888$ m/s and a defect at 5 cm depth.
  - Thin layer with low modulus (modulus of air, modulus of base); and
  - Interface element with R factor of 0.01 and 0.22.
- The size (horizontal extent) of the delamination was investigated with HMA $V_s = 888$ m/s and a defect at 5 cm depth.
  - The test array directly above the delamination;
  - The test array partially in front of the delamination; and
  - The test array partially after the delamination.

Results

Control Model

The presented results are so-called dispersion images based on a multichannel analysis of all types of seismic waves propagating along the surface of a pavement. The dispersion images

Table 3.1. Properties for Pavement Profile—Control Model

Material	Unit Weight (kN/m³)	Poisson's Ratio	V_p (m/s)	V_s (m/s)	Layer Thickness (m)
HMA	23	0.35	1,850	888	0.15
Base	19	0.35	407	195	0.25
Subgrade	15	0.35	324	156	0.6

Note: V_p = phase velocity.

Table 3.2. Parameter Study for Evaluating Pavement with Delaminations

Variable	Description
Depth of defect	At 5, 10, and 15 cm
Modulus of HMA	With $V_s = 400$, 888, and 1,250 m/s
Bonding condition	Thin layer filled with air or base
	Interface with strength reduction $R = 0.01$ and 0.22
Size of defect	Full extent or partial coverage of test array

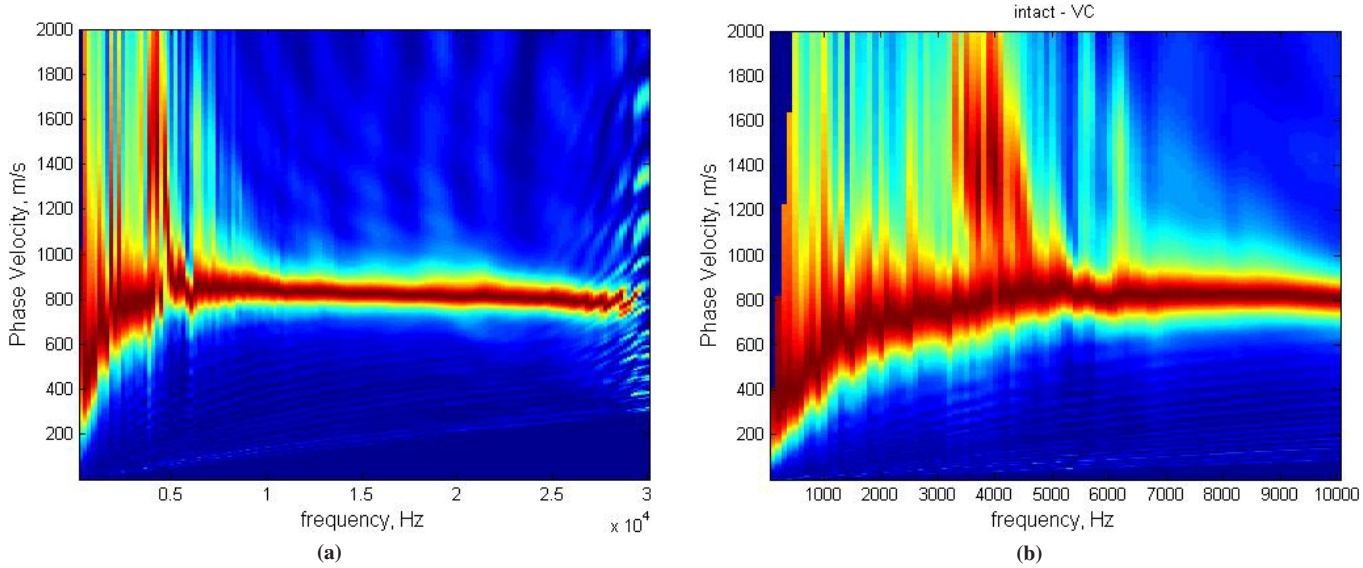

Figure 3.21. Dispersion images of intact pavement with V_s = 888 m/s for HMA (a) with pulse frequency of 20 kHz and (b) with pulse frequency of 10 kHz.

are a form of 3-D power spectrum in which the surface wave phase velocity versus frequency (dispersion) of the propagating waves is displayed on the horizontal axes, and the energy present at each velocity-frequency pair is displayed via a color coding, with the cold colors corresponding to low energy, and the hot colors corresponding to high energy. A concentration of hot energy over a narrow band represents a normal mode of wave propagation, and the velocity-frequency pairs along the peak of the narrow band are typically referred to as the dispersion curve in surface wave testing. A dispersion curve is a relationship showing how the surface wave phase velocity of a layered material changes with frequency (or wavelength). In this study, the dispersion images are obtained via a cylindrical beamforming algorithm, which essentially transforms the raw signals (i.e., the time signatures obtained from PLAXIS) from the time-space domain to the velocity-frequency domain, by taking into account the cylindrically propagated wave field.

In this study, intact (no defect) pavement models were treated as control models for comparison with various defect models. It was found that the dispersion images from the intact pavement profiles (Figures 3.21 to 3.23) did not display

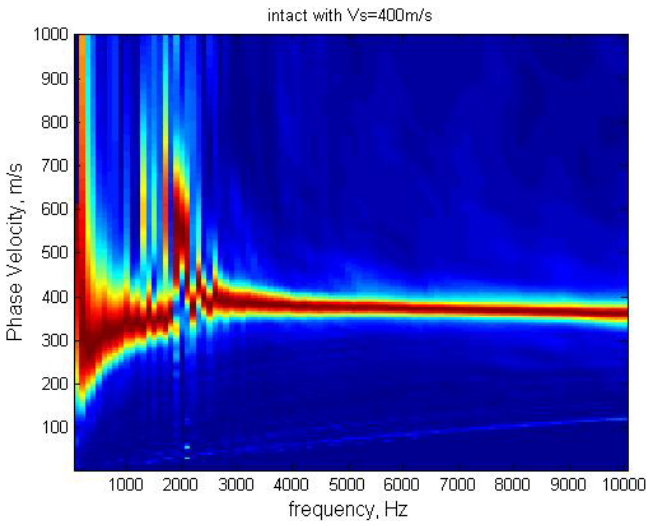

Figure 3.22. Dispersion image of intact pavement with V_s = 400 m/s for HMA with pulse frequency of 10 kHz.

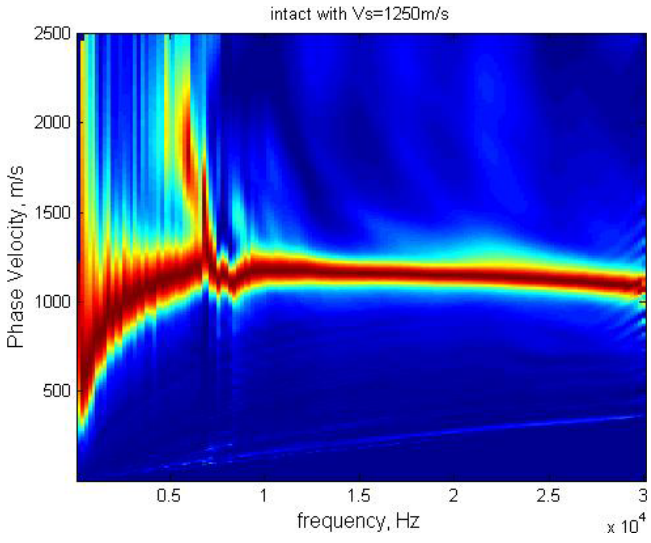

Figure 3.23. Dispersion image of intact pavement with V_s = 1,250 m/s for HMA with pulse frequency of 20 kHz.

a continuous band of normal mode energy, but displayed several branches, especially at low frequencies. It is believed that such discontinuities correspond with interaction between the high-modulus surface layer and the base and subgrade in the pavement system (Rydén 2004). However, at high frequencies, a narrow band (dispersion curve) tends to converge to a single value, which corresponds to the Rayleigh wave velocity of the very top HMA layer (slightly lower than V_s and according to Poisson's ratio).

Depth of Defect

To study the effect of a defect, total debonding is introduced at depths of 5, 10, and 15 cm, respectively, across the full horizontal width of the model, and is intended to represent complete shallow, intermediate, and deep delaminations in reality. Note that for the cases of 5 cm and 10 cm, the defect is in the HMA layer; for the case of 15 cm, the defect is right at the interface between HMA and base. Total debonding is modeled as either an extremely thin layer filled with air, or via an interface element with the strength reduction factor set to its minimum ($R = 0.01$). The strength reduction factor (R) is a parameter employed in PLAXIS to control the degree of continuity between two adjacent surfaces, having a maximum value of 1 (complete continuity) and a minimum value of 0.01 (nearly independent or frictionless).

To illustrate the model, a HMA shear wave velocity of 888 m/s is considered, and the dispersion images for the defect models are shown in Figures 3.24 to 3.26. Note that the corresponding dispersion image for the intact model has been shown in Figure 3.21. First, it should be observed that the two approaches to modeling the defect result in very similar dispersion images at all defect depths considered; that is, image (a) and image (b) in Figure 3.21 are nearly the same. For this case of total debonding, the HMA layer above can freely slide along the interface, and this layer can essentially be thought of as a free plate. Hence, the results can be explained by Lamb's free plate model as shown in Figure 3.27. Lamb waves refer to those in thin plates (with planar dimensions being far greater than that of the thickness, and with the wavelength being on the order of the thickness) that provide upper and lower boundaries to guide continuous propagation of the waves. Lamb waves consist of symmetric (Si) and antisymmetric (Ai) modes, which can coexist when excited. The antisymmetric modes correspond to bending waves in the plate, and the symmetric modes correspond to quasi-longitudinal waves in the plate. Figure 3.28a plots the Lamb wave dispersion curves in a free plate. At high frequencies, the A0 and S0 modes merge together, and the convergent velocity corresponds to the Rayleigh wave velocity of the free plate. For example, in Figure 3.24, it is clear that the dominating mode is the fundamental antisymmetric mode (A0) of Lamb waves. In addition, there is another branch trying to merge with A0 from above, which is expected to be the fundamental symmetric mode (S0).

Second, on comparing the intact model from Figure 3.21 with the defect model in Figure 3.24, another important feature is revealed: at low frequencies the dispersion curve (narrow band) of the delaminated case appears to be much smoother, and this smooth curve is interpreted as the A0 mode. The dispersion image of the intact model has the discontinuities associated with the base and subgrade interaction, but the defect model is free of these low-frequency effects due to the debonding. For the cases of delamination at 10 cm (Figure 3.25), the dispersion image shows discontinuities at approximately 6 kHz and 11 kHz. The wavelengths are to

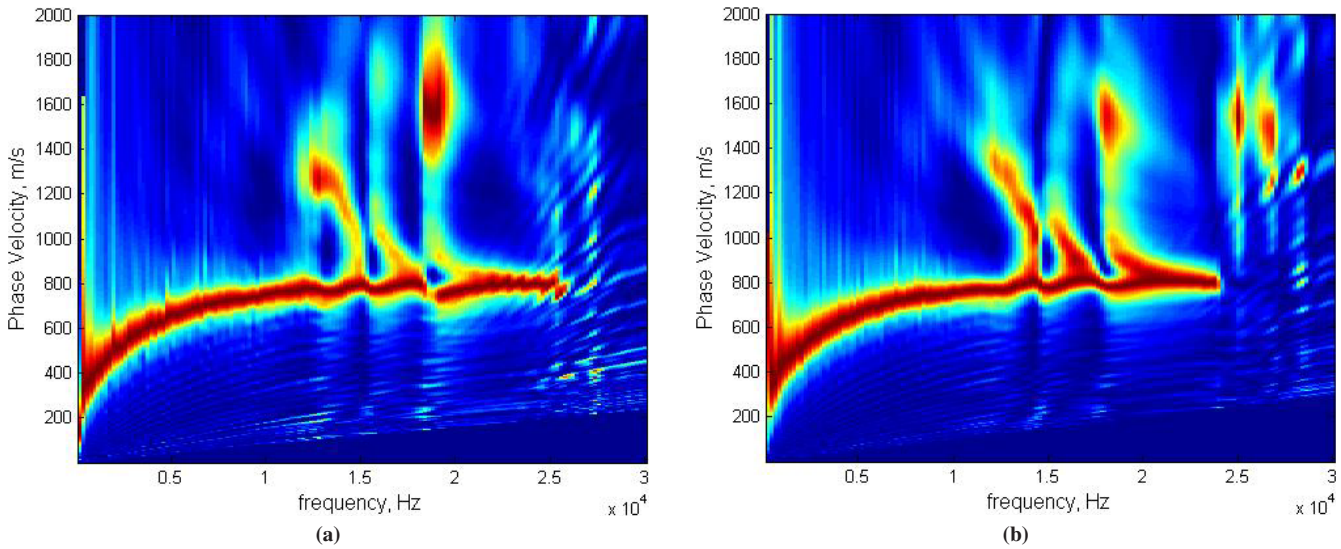

Figure 3.24. Dispersion images of total delamination at a depth of 5 cm for (a) air and (b) R = 0.01.

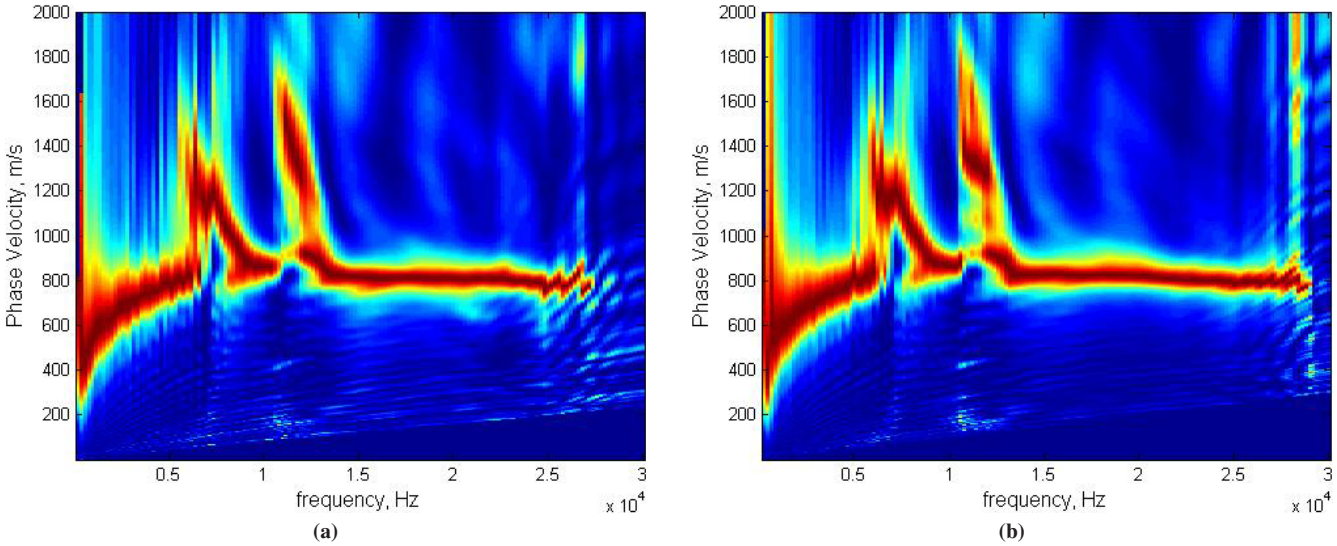

Figure 3.25. Dispersion images of total delamination at a depth of 10 cm for (a) air and (b) R = 0.01.

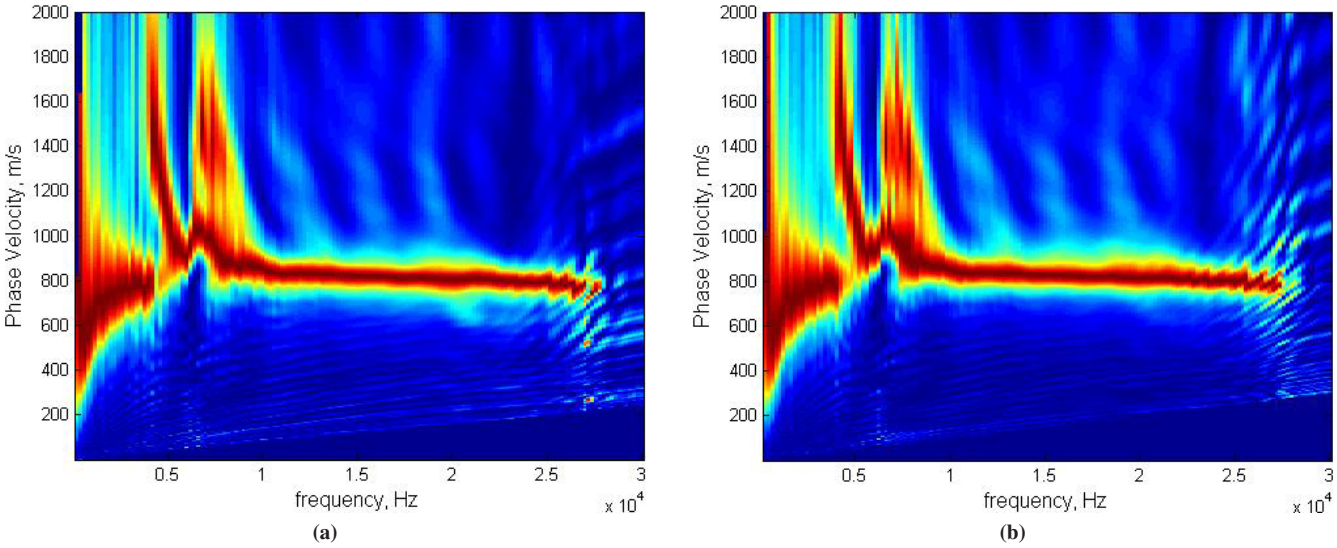

Figure 3.26. Dispersion images of total delamination at a depth of 15 cm for (a) air and (b) R = 0.01.

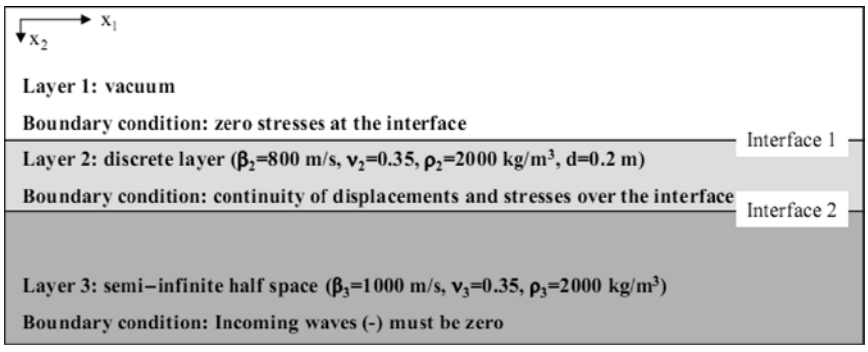

Source: Rydén 2004.

Figure 3.27. Lamb's free plate model.

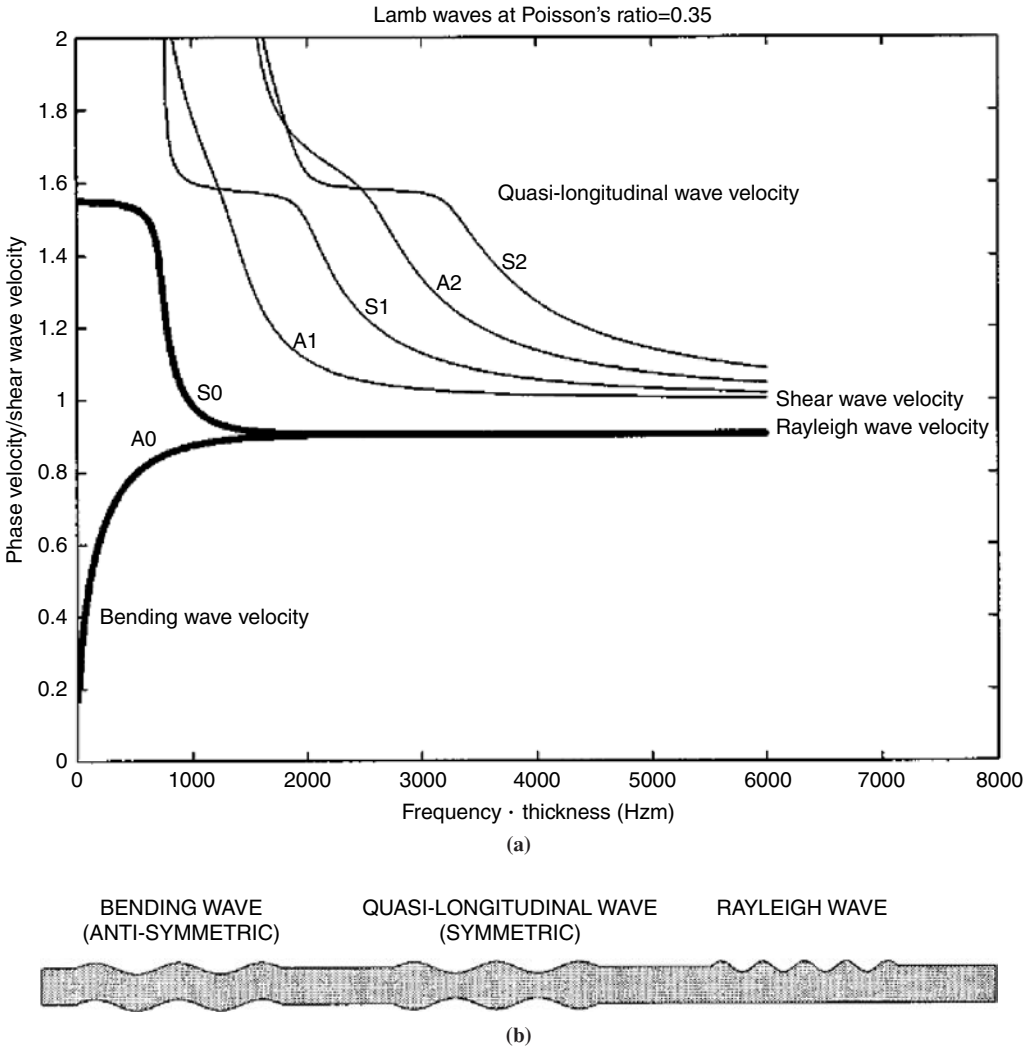

Source: Rydén 2004.

Figure 3.28. (a) Lamb wave dispersion curves in free plate and (b) particle motion showing different types of waves in the model.

some extent related to the depth of the delamination. For the cases of delamination at 15 cm (Figure 3.26), the dispersion image shows discontinuities at approximately 4 kHz and 6 kHz. It is observed that the discontinuities are more evident than in the previous cases; that is, as the delamination goes deeper, the S0 mode becomes clearer. Alternatively stated, the dispersion image becomes similar to the intact case as the delamination goes deeper; thus, the surface wave method may not be very sensitive to deep delaminations.

HMA Modulus

Next, the effect of elastic modulus of the HMA layer is investigated. It has been demonstrated that both approaches to modeling delamination yield very similar results. Considered here are only the cases with total debonding at a depth of 5 cm and modeled with a thin layer filled with air. Elastic moduli of the HMA layer are changed such that the shear wave velocities are 400, 888, and 1,250 m/s, accordingly.

Figure 3.28 shows clearly that the dispersion curve is dominated by both the A0 and S0 modes of Lamb waves. Examining Figures 3.29 to 3.31 reveals that as the modulus of HMA increases, the S0 mode becomes weaker. In Figure 3.31, the dispersion image is almost dominated by the A0 mode alone. It is also interesting to notice that for different moduli of HMA, the fundamental symmetric mode (S0) appears at a higher starting frequency. For example, S0 appears from about 5.5 kHz for the HMA in Figure 3.30, and vaguely from about 17.5 kHz for the stiffest HMA in Figure 3.31. This result makes sense because Lamb wave

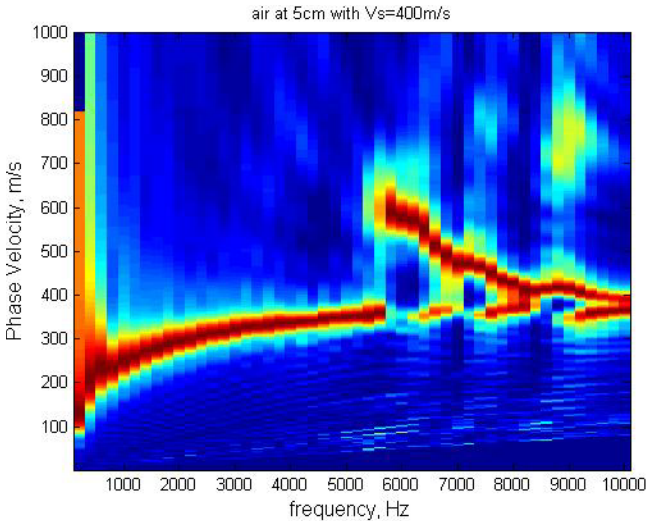

Figure 3.29. Dispersion image of total delamination at a depth of 5 cm with HMA V_s = 400 m/s.

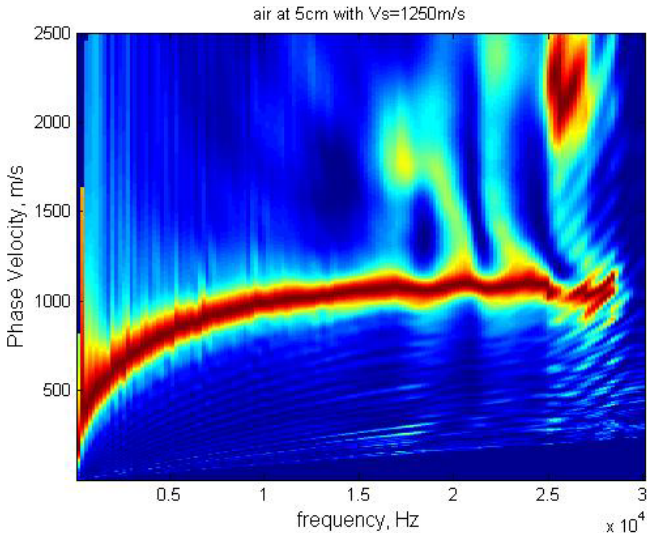

Figure 3.31. Dispersion image of total delamination at a depth of 5 cm with HMA V_s = 1,250 m/s.

dispersion is a function of plate modulus, as well as of plate thickness and Poisson's ratio.

Degree of Defect

Total debonding between HMA lifts is probably rare in reality, and most often delaminations are characterized by weak bonds between interfaces. Therefore, partial delaminations are investigated by modeling the thin layer with a low modulus (base material) that is higher than air. To test whether the interface approach would render similar results, the strength reduction factor is set to 0.22, which produces results comparable to the base-filled thin layer. The results are presented for HMA V_s = 888 m/s and the defect at a depth of 5 cm.

First, for aid in the comparison, Figure 3.32 is a repeated version of Figure 3.24, and Figure 3.33 displays the dispersion image for a thin layer with low modulus higher than air. After comparing Figure 3.33 to Figure 3.32, it is evident that with the partial delamination the S0 mode nearly disappears. Moreover, Figure 3.33 shows a discontinuous low-frequency

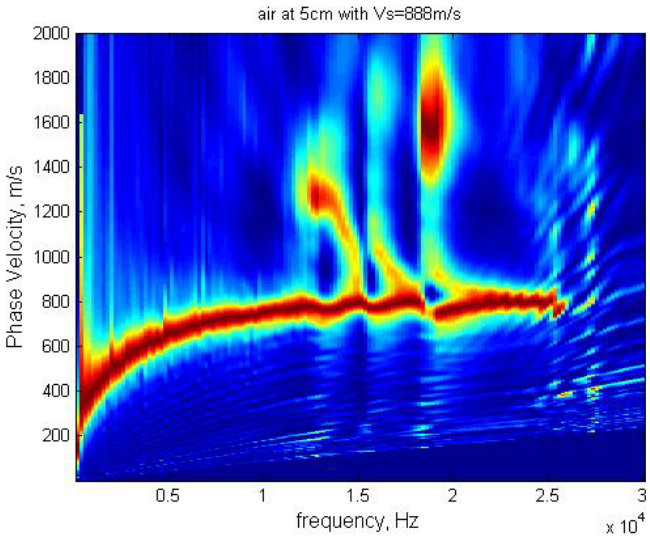

Figure 3.30. Dispersion image of total delamination at a depth of 5 cm with HMA V_s = 888 m/s.

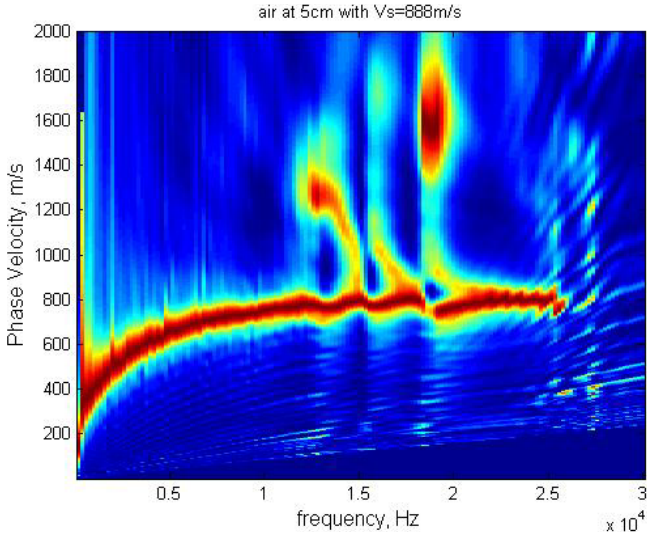

Figure 3.32. Dispersion image of total delamination for thin layer filled with air at a depth of 5 cm and HMA V_s = 888 m/s.

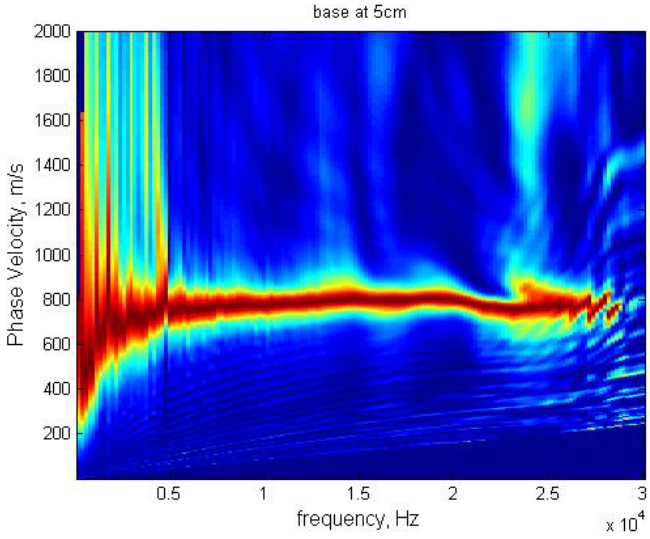

Figure 3.33. Dispersion image of partial delamination for thin layer filled with base material at a depth of 5 cm.

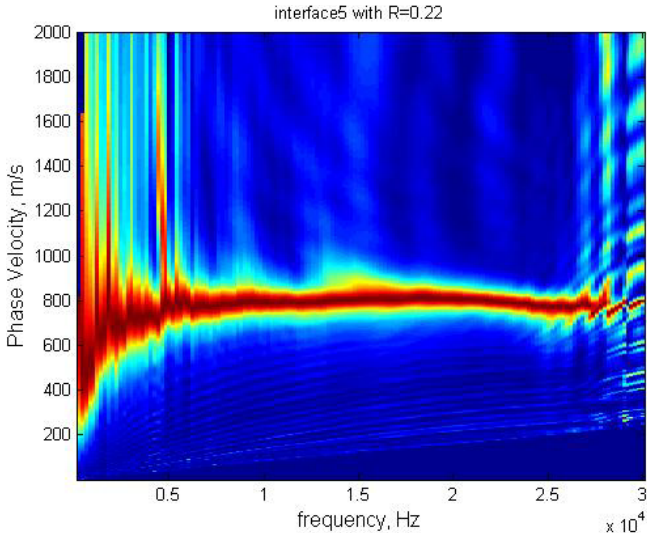

Figure 3.35. Dispersion image of partial delamination for interface element with R = 0.22.

response and a slight drop in phase velocity at high frequencies. It is known that the low-frequency discontinuity is the feature of an intact pavement profile. It is inferred that the slight drop in phase velocity at high frequencies may be related to the base-filled defect.

Second, a very similar comparison is presented in Figures 3.34 and 3.35 for the interface approach, including the lack of the S0 mode and a low-frequency discontinuity. Furthermore, it should be noted that the discontinuous low-frequency responses in Figures 3.33 and 3.35 are slightly different from that in Figure 3.21, which implies that a shallow partial delamination gives rise to differences in the dispersion image at both high and low frequencies.

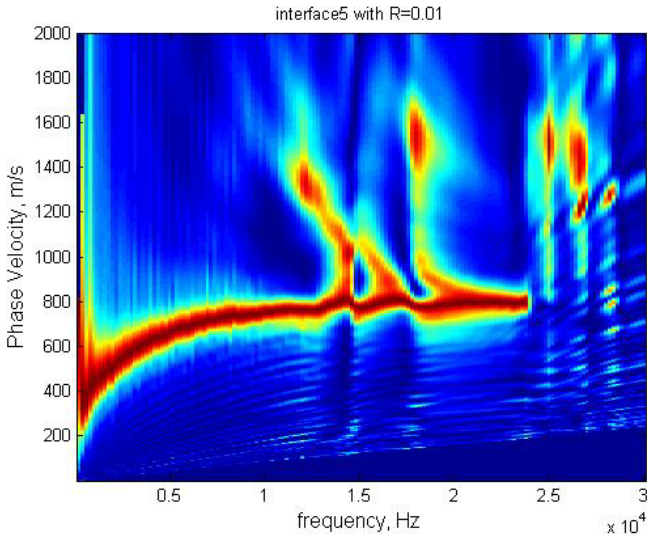

Figure 3.34. Dispersion image of total delamination for interface element with R = 0.01.

Defect Size

It is likely that delaminations are typically localized in size, and thus do not extend horizontally across the entire interface. Given a delaminated pavement specimen, the research team does not know where the delamination has occurred. Thus, if a test array is placed on the surface, the test array can by chance fully cover the size of the defect, or may just partially cover the delamination. Therefore, to simulate a real MASW test on pavement, three possible situations are considered: (1) an array right above the defect, (2) an array partially over the defect with the source and part of the array in front, and (3) an array with the source and part of the array over the defect. For full coverage, Case 1, the delamination length is set to be 1 m long horizontally, from 0.3 m to 1.3 m in the model (Figure 3.19). For partial coverage, the delamination size is set to be 0.7 m long. The delamination extends from 0.85 to 1.55 m for Case 2 and from 0 to 0.7 m for Case 3. For all cases, the receiver array configuration is as shown in Figure 3.20, from 0.5 m to 1.1 m, and with the source at 0. The results are presented for HMA V_s = 888 m/s, and the defect at a depth of 5 cm.

First, for aid in the comparison, Figure 3.36 is a repeated version of Figures 3.24b and 3.34: total debonding modeled with an interface element. For Case 1, in comparison with Figure 3.36, the dispersion image shown in Figure 3.37 contains discontinuities at low frequencies and no S0 mode. This can be explained from the deformed mesh at the end-of-time steps shown in Figure 3.41. Because the delamination starts from 0.3 m and

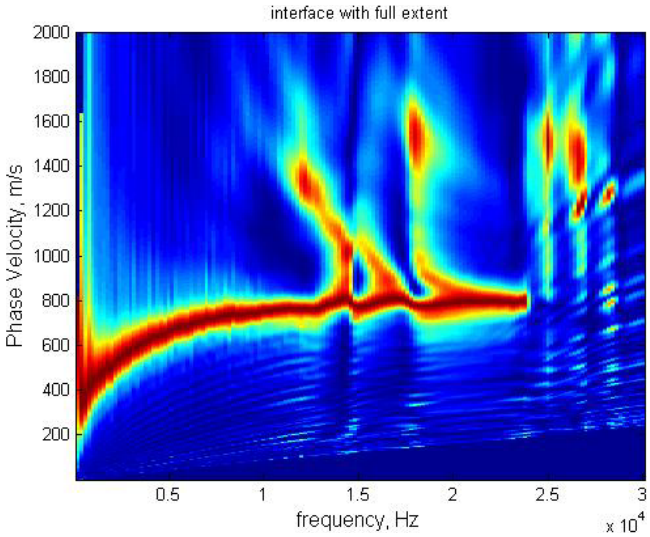

Figure 3.36. Dispersion image of total delamination with full interface extent.

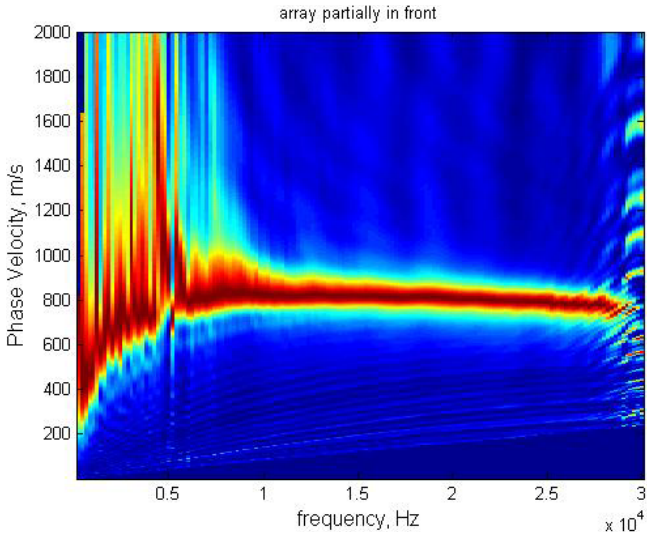

Figure 3.38. Dispersion image of total delamination with partial array coverage (Case 2).

ends at 1.3 m, it is constrained from both ends. Therefore, a Lamb wave approximation is not appropriate in this case.

For Case 2 shown in Figure 3.38, the dispersion image appears similar to the intact case previously presented in Figure 3.21, with some differences noted at low frequencies. Due to the fact that most of the sensors collect signals from an intact profile from 0.5 m to 0.85 m, the dispersion image at high frequencies is nearly the same as that in Figure 3.21. Thus, it is inferred that the slight low-frequency difference is created by sensors that are placed above the delamination.

For Case 3 shown in Figure 3.39, the dispersion image generally looks similar to the total delaminated case in Figure 3.36, with a noticeable S0 mode at high frequencies. However, it also displays a discontinuous A0 mode at low frequencies. In addition to comparing dispersion images, it is helpful to also review the deformed meshes. Figure 3.40 plots the deformed mesh for the fully delaminated case corresponding to the dispersion curve in Figure 3.36. With a full interface extension for the delamination, the flexural mode of vibration dominates. However, in Figures 3.41 and 3.42, the deformation is more constrained due to the confinement from the boundaries. In Figure 3.43, again the flexural mode dominates, and it happens right above the delamination. In summary, the interpretation

(text continued on page 37)

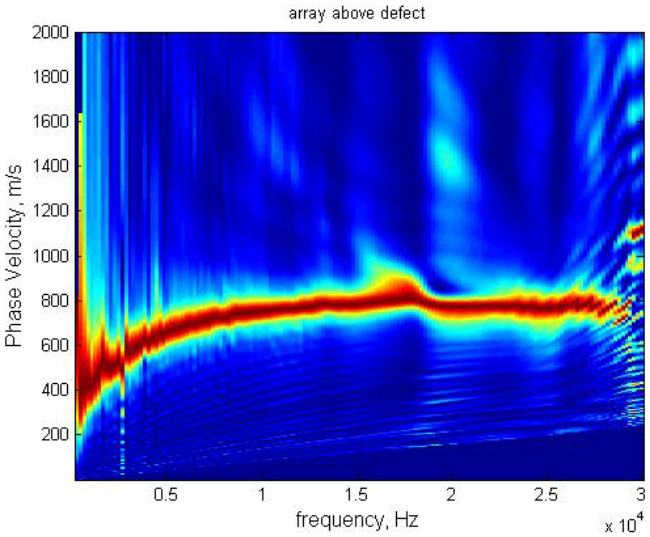

Figure 3.37. Dispersion image of total delamination with full array coverage (Case 1).

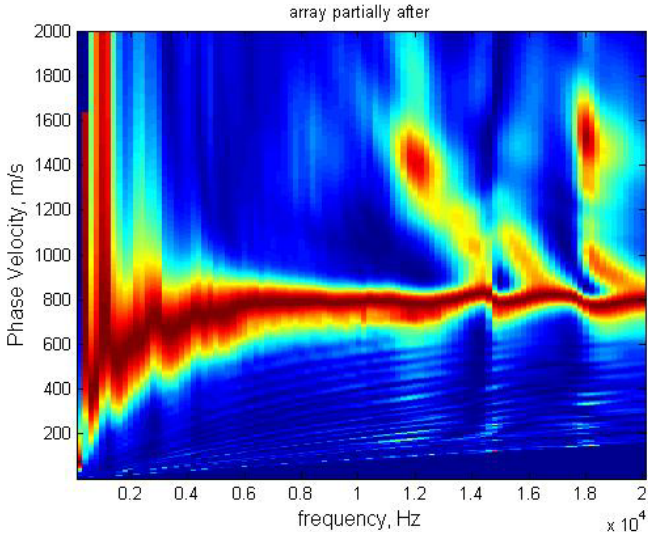

Figure 3.39. Dispersion image of total delamination with partial array coverage (Case 3).

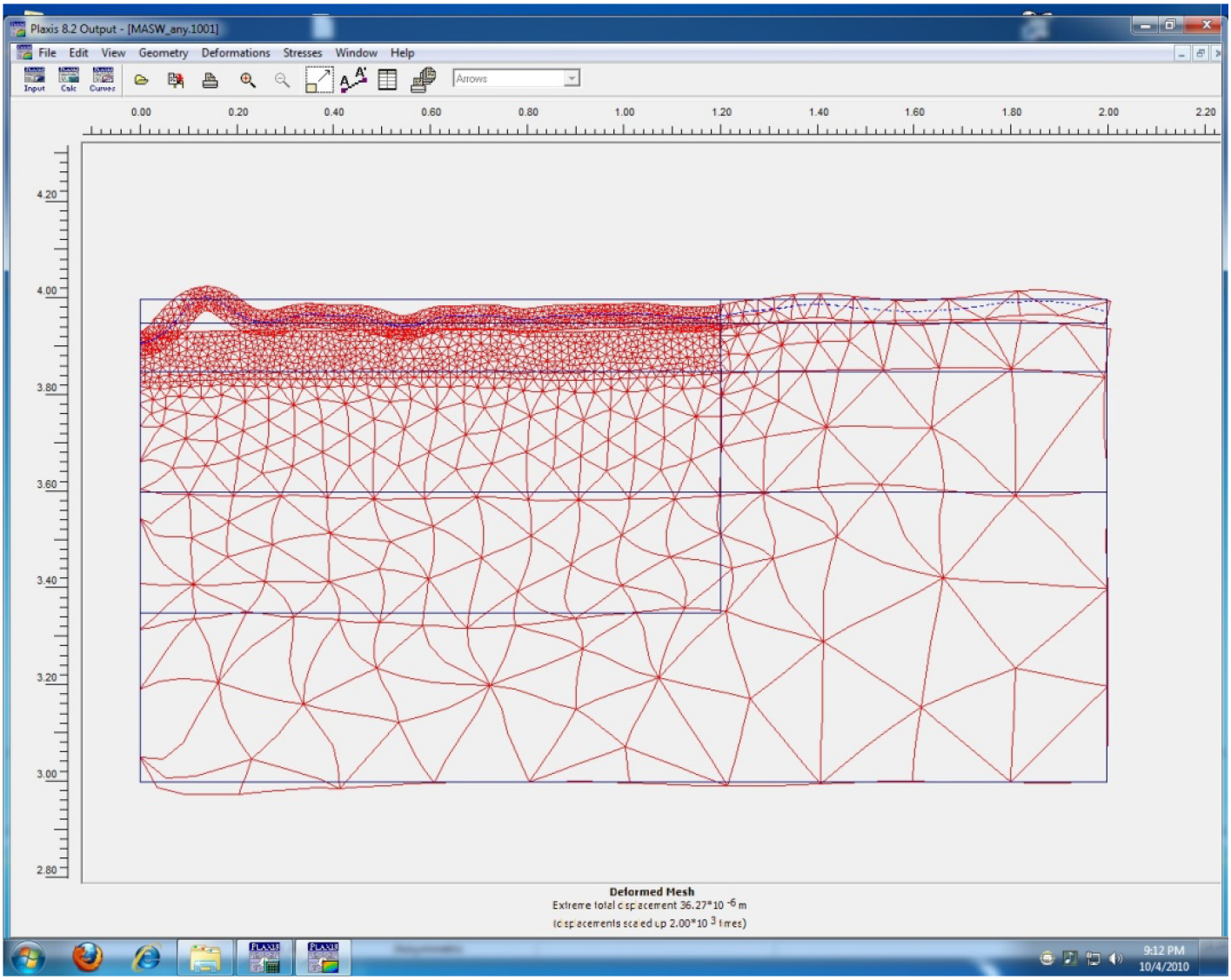

Figure 3.40. Deformed mesh of total delamination with full interface extension.

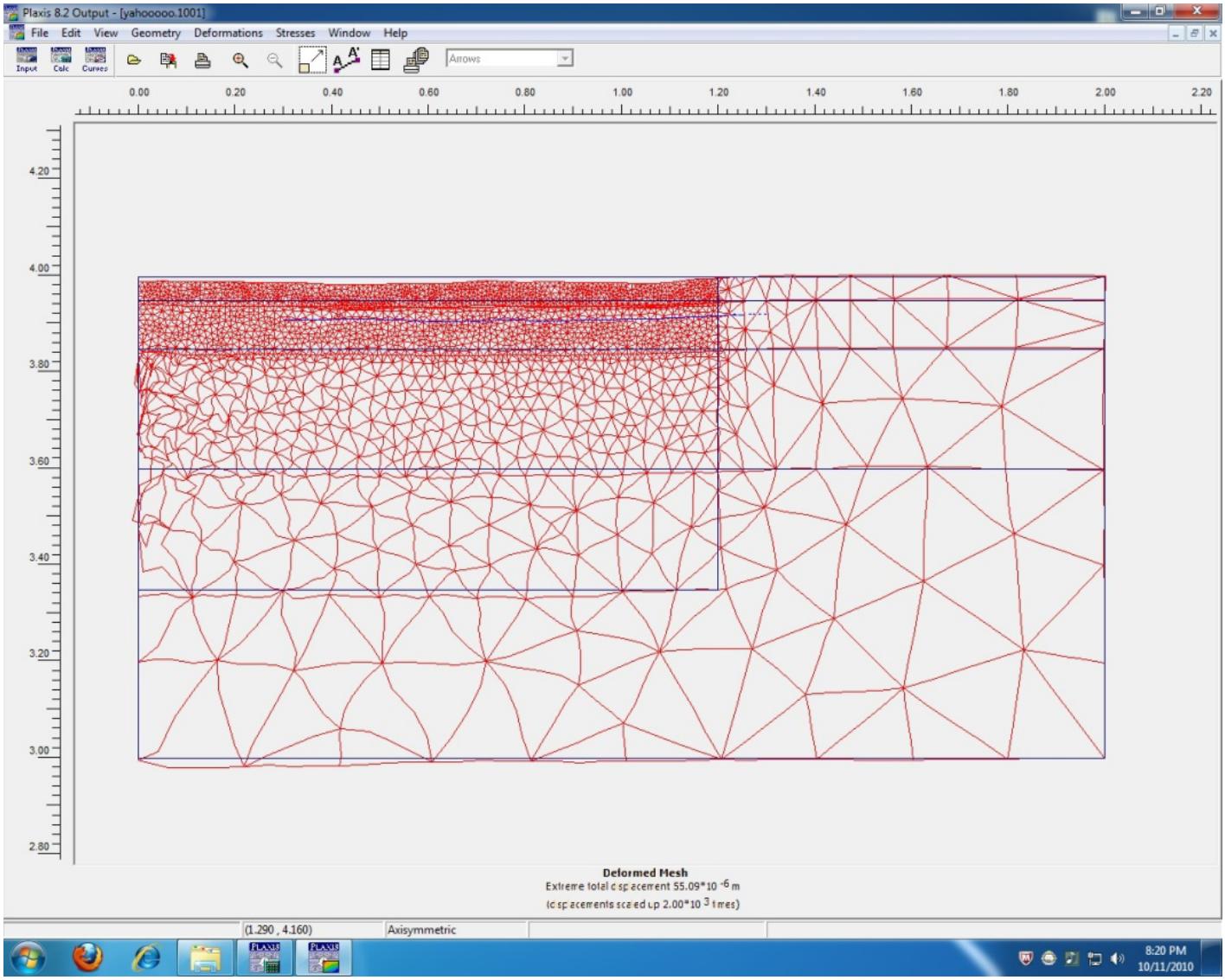

Figure 3.41. Deformed mesh of partial delamination with full array coverage (Case 1).

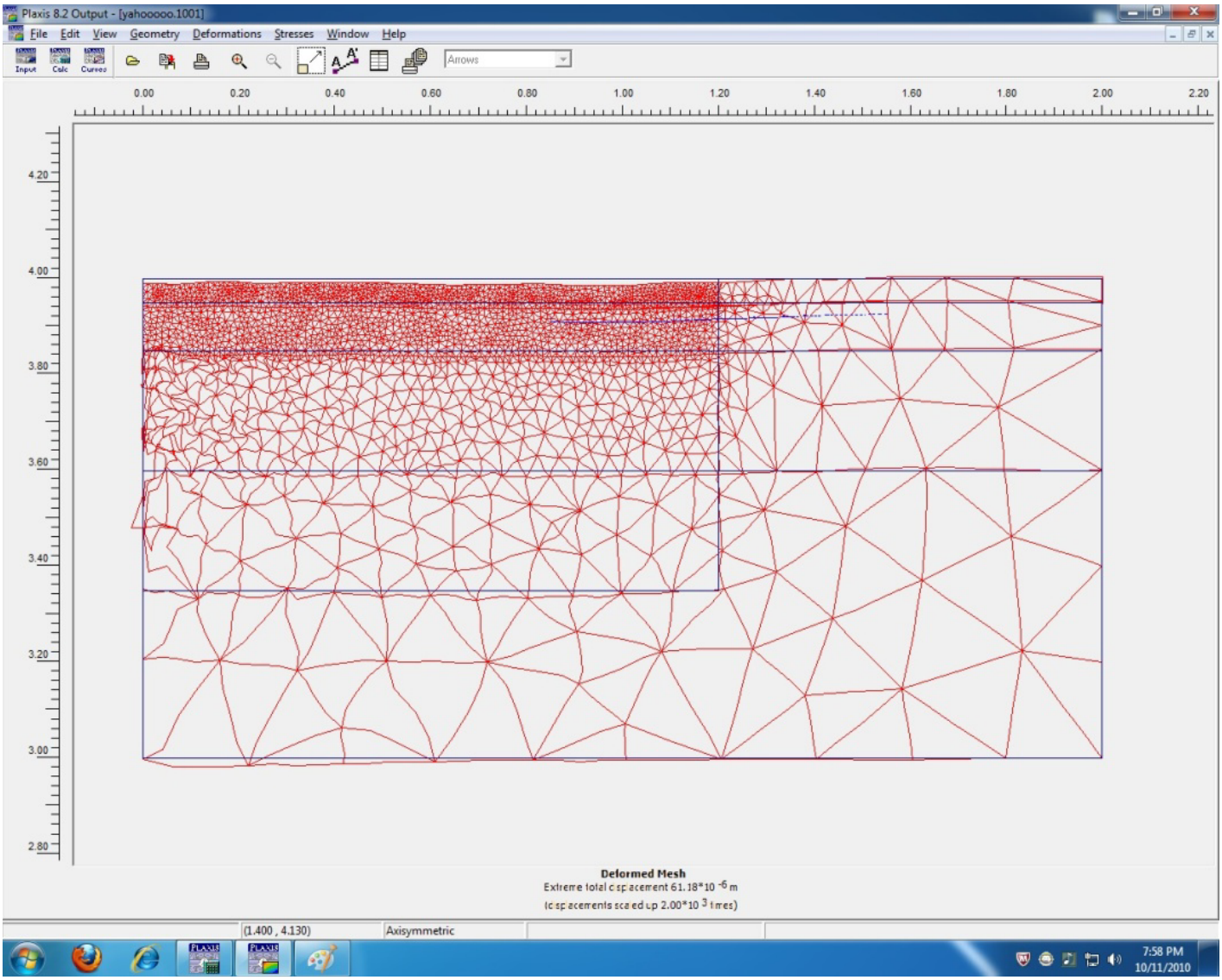

Figure 3.42. Deformed mesh of partial delamination with partial array coverage (Case 2).

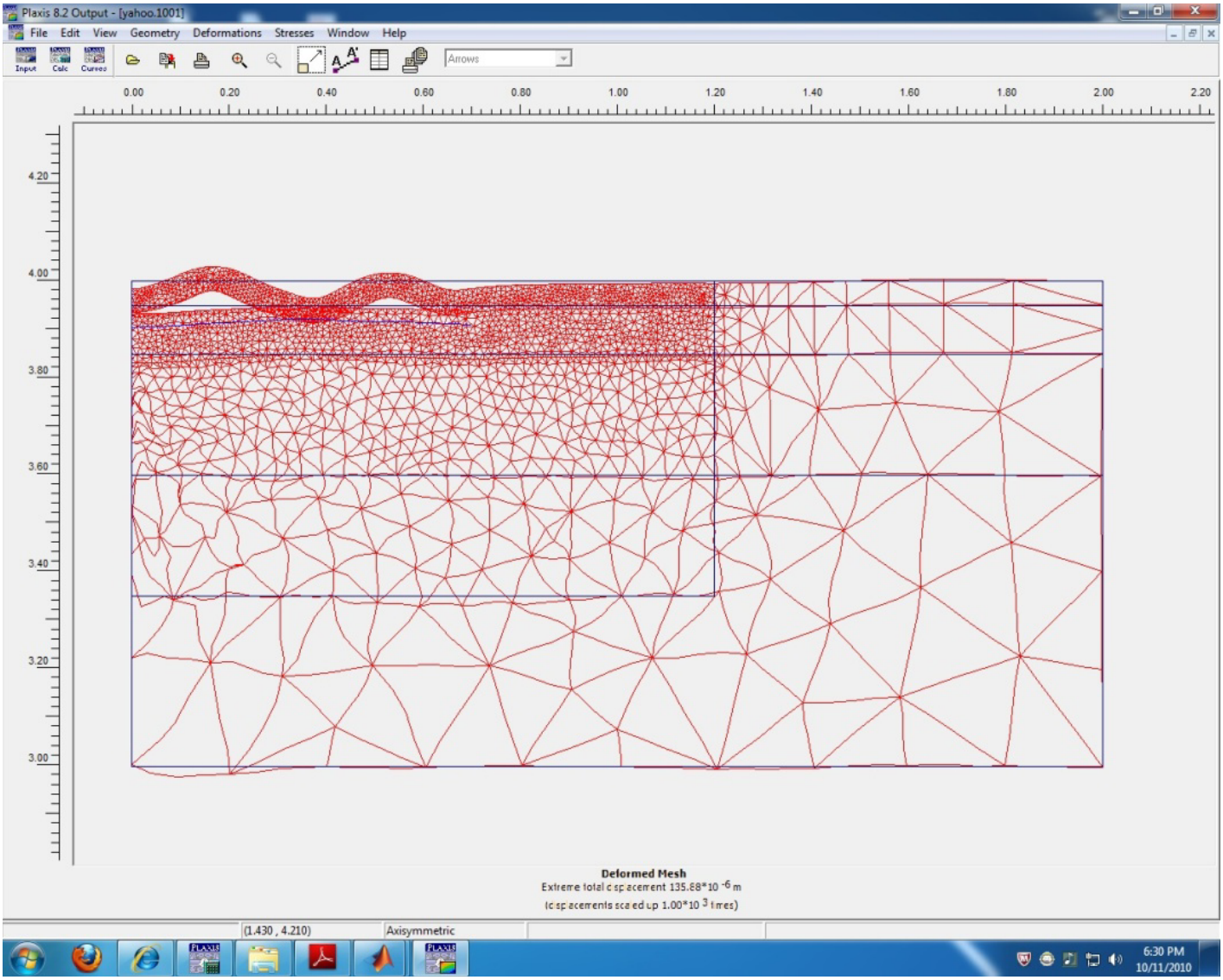

Figure 3.43. Deformed mesh of partial delamination with partial array coverage (Case 3).

(*continued from page 33*)
of dispersion images significantly depends both on the size of the delamination and the array configuration.

Conclusions

A surface wave technique has been applied to detect pavements with delamination. All results are based on finite element simulation and presented in the form of dispersion images. On the basis of differences in the dispersion images, the following conclusions were reached:

1. Delamination in HMA pavements can be effectively simulated as either a thin layer with low modulus or by the interface element between layers.
2. In general, the shallow full-scale delamination is easier to detect and can be explained by the Lamb wave approximation. The deep and small-scale delaminations are more difficult to detect.
3. Array configuration plays a significant role in interpreting differences in dispersion images caused by localized delaminations.

References

Munoz, D. 2009. *Finite Element Modeling of Nondestructive Test Methods Used for Detection of Delamination in Hot Mix Asphalt Pavements.* MS thesis, University of Texas at El Paso.

Rydén, N. 2004. *Surface Wave Testing on Pavements.* PhD dissertation, Lund University, Lund, Sweden.

CHAPTER 4

Theoretical Models for Mechanical Wave Technology: Deflection-Based Approach

The research presented in this chapter was carried out by Dr. Halil Ceylan and Dr. Sunghwan Kim at Iowa State University.

Seismic waves move in different ways through and around the earth and are of two primary types (Wehausen and Laitone 2002):

- Body waves
  - P-waves (primary waves or pressure waves or compression waves); and
  - S-waves (secondary waves or shear waves),
- Surface waves
  - Love waves; and
  - Rayleigh waves

Seismic pavement nondestructive testing (NDT) uses surface wave propagation to estimate the structural properties (thickness and stiffness) of layered pavement systems (Rydén 2004). Dynamic Young's modulus (E) and Poisson's ratio (ν) are directly calculated from measured seismic velocities by using fundamental relationships. Seismic NDT technology, based on the principle of generation and detection of stress waves, has been shown to produce relatively high-resolution modulus profiles compared to most pavement NDT methods.

The introduction of the spectral analysis of surface waves (SASW) method (Nazarian 1984) has especially led to widespread acceptance of seismic pavement NDT methods and the development of standard field protocols (Nazarian et al. 1995). Two well-known automated seismic pavement NDT devices include the seismic pavement analyzer and the portable seismic pavement analyzer (Nazarian 1984; Nazarian et al. 1993; Baker et al. 1995).

Seismic pavement testing methods involve acquiring raw data on pavement surface, which are simply the time histories of the impact source and the surface deformation. These time records, which describe the pavement structure in terms of P-waves, S-waves, Rayleigh waves, and bending modes, can be analyzed in five different ways. Each of these five methods has its own strengths and limitations as shown in Table 4.1 (Yuan et al. 1999). The arrivals of compression, shear, and Raleigh waves are shown in Figure 4.1 for typical time records from two sensors placed 150 mm apart on a thick asphalt pavement.

The dispersive nature of surface waves in a layered medium is used to assess the elastic moduli of pavement layers with the following procedure (see Figure 4.2):

1. Acquire data at the surface of a pavement (measured dispersion curve).
2. Evaluate the measured experimental dispersion curve.
3. Evaluate shear wave velocity (V_s) with depth profile from the experimental dispersion curve through inverse analysis.

Rydén et al. (2004) developed a multimodal approach to seismic pavement testing by using the complete phase velocity spectrum instead of discrete dispersion waves, after concluding that the earlier techniques oversimplified the nature of wave propagation along the pavement surface.

Rydén and Mooney (2009) conducted an experimental and numerical study to explore low-strain modulus extraction from seismic waves during the lightweight deflectometer (LWD) test and demonstrated the usefulness of the LWD as a source for surface seismic measurements. Figure 4.3 displays the comparison of strain levels from surface waves by using the conventional small hammer source and the LWD source on soft subgrade (Rydén and Mooney 2009).

Table 4.1. Pavement Properties Measured with Different Seismic Methods[a]

Method	Primary Use	Strength	Weakness
Time Record Analysis	Modulus of top layer	Rapid to perform Simple data reduction	Results may be affected by underlying layers Sensitive to surface condition
Ultrasonic Surface Waves (USW)	Modulus of top layer	Sensitive to properties of top layer Rapid to perform Layer specific results	In manual mode, data reduction is complex
Impact Echo (IE)	Thickness of top layer or depth to delaminated interface	Can determine thickness of the layer Sensitive to delaminated interfaces	Substantial contrast between the modulus of two adjacent layers is needed to be effective For multicourse pavements, at least one core is needed for calibration Applies only to pavements with thicker top layer
Impulse Response	Modulus of subgrade reaction of foundation layers or overall modulus of a pavement	Powerful tool for rapidly locating weak spots in a pavement May be used to estimate depth to stiff layer (in progress)	For flexible pavements, the contributions of different layers are unknown Results are affected by depth to rigid layer and water table
Spectral Analysis of Surface Waves (SASW)	Modulus and thickness of each layer	Provides the modulus profile in a comprehensive manner More robust than deflection-based methods	In manual mode, testing and data reduction are time-consuming and complex Automated analysis applicable only to simple structure

[a] Yuan et al. 1999.

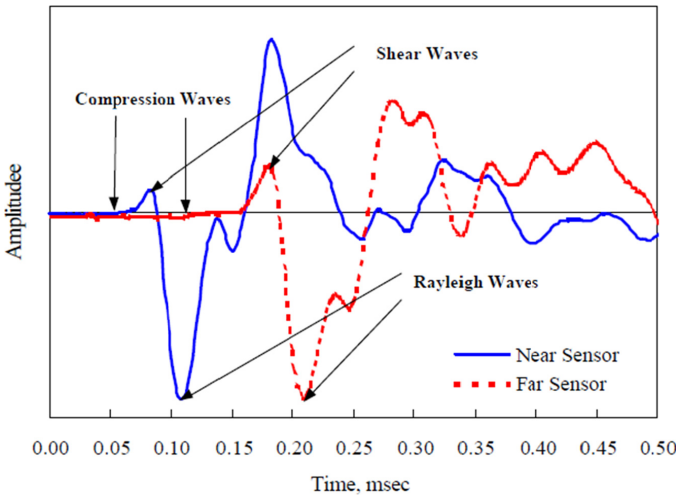

Source: Yuan et al. 1999.

Figure 4.1. Typical time domain records from seismic test on thick asphalt pavement.

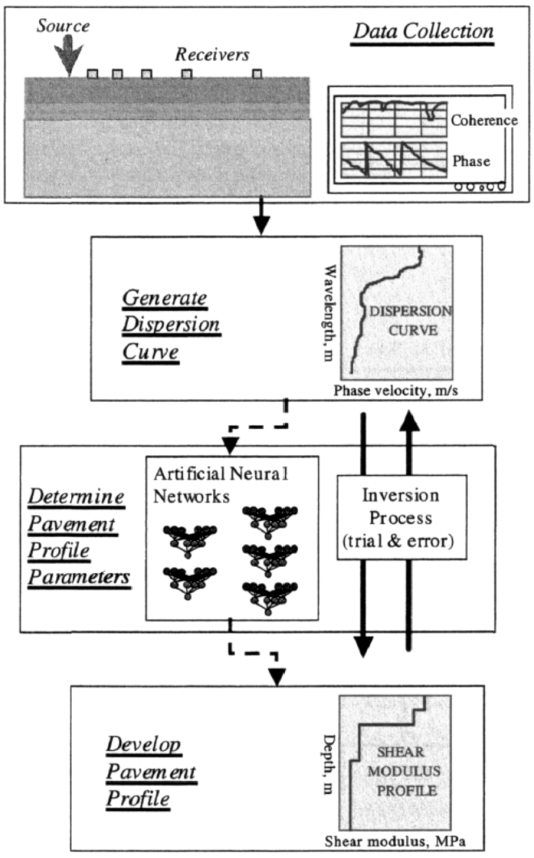

Source: Wu et al. 2002.

Figure 4.2. SASW procedure flowchart.

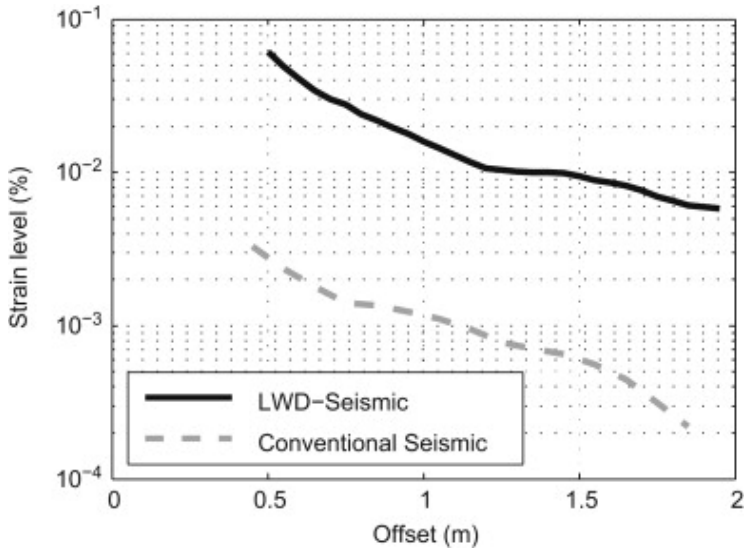

Source: Rydén and Mooney 2009.

Figure 4.3. Comparison of strain levels from surface waves using conventional small hammer source and LWD source on soft subgrade.

References

Baker, M. R., K. Crain, and S. Nazarian. 1995. *Determination of Pavement Thickness with a New Ultrasonic Device.* Research Report 1966-1, Center for Geotechnical and Highway Materials Research, University of Texas at El Paso.

Nazarian, S. 1984. *In situ determination of soil deposits and pavement systems by spectral analysis of surface waves method.* PhD dissertation. University of Texas at Austin.

Nazarian, S., M. R. Baker, and K. Crain. 1993. *SHRP-H-375: Fabrication and Testing of a Seismic Pavement Analyzer.* Transportation Research Board of the National Academies, Washington, D.C.

Nazarian, S., D. Yuan, and M. Baker. 1995. *Rapid Determination of Pavement Moduli with Spectral-Analysis-of-Surface-Waves Method.* Research Report 1243-1, The University of Texas at El Paso.

Rydén, N., C. B. Park, P. Ulriksen, and R. D. Miller. 2004. Multimodal Approach to Seismic Pavement Testing. *Journal of Geotechnical and Geoenvironmental Engineering,* 130, No. 6, pp. 636–645.

Rydén, N. 2004. *Surface Wave Testing of Pavements.* PhD dissertation. Lund Institute of Technology, Lund, Sweden.

Rydén, N., and M. A. Mooney. 2009. Analysis of surface waves from the light weight deflectometer. *Soil Dynamics and Earthquake Engineering,* 29, No. 7, pp. 1134–1142.

Wehausen, J. V., and E. V. Laitone. 2002. *Surface waves.* Springer, Berlin.

Wu, H., I. Wang, I. Abdallah, and S. Nazarian. 2002. A rapid approach to interpretation of SASW results. *Proc., 6th BCRA Conference 2002,* Lisbon, Portugal.

Yuan, D., S. Nazarian, D.-H. Chen, and M. McDaniel. 1999. Use of Seismic Methods in Monitoring Pavement Deterioration During Accelerated Pavement Testing with TxMLS. *Proc., First International Conference on Accelerated Pavement Testing (APT),* Reno, Nevada.

Related SHRP 2 Research

Nondestructive Testing to Identify Concrete Bridge Deck Deterioration (R06A)

Evaluating Applications of Field Spectroscopy Devices to Fingerprint Commonly Used Construction Materials (R06B)

Using Infrared and High-Speed Ground-Penetrating Radar for Uniformity Measurements on New HMA Layers (R06C)

Real-Time Smoothness Measurements on Portland Cement Concrete Pavements During Construction (R06E)

Assessment of Continuous Pavement Deflection Measuring Technologies (R06F)

Mapping Voids, Debonding, Delaminations, Moisture, and Other Defects Behind or Within Tunnel Linings (R06G)